ACSNANO

www.acsnano.org

ARTICLE

Nanoparticle-Mediated RNA Therapy Attenuates Nonalcoholic Steatohepatitis and Related Fibrosis by Targeting Activated Hepatic Stellate Cells

Chenshuang Zhang, Yilong Teng, Fengqiao Li, William Ho, Xin Bai, Xiaoyang Xu,* and Xue-Qing Zhang*

Cite This: *ACS Nano* 2023, 17, 14852−14870

Read Online

ACCESS | Metrics & More | Article Recommendations | Supporting Information

ABSTRACT: Chronic liver injury and inflammation triggered by metabolic abnormalities initiate the activation of hepatic stellate cells (HSCs), driving fibrosis and parenchymal dysfunction, culminating in disorders such as nonalcoholic steatohepatitis (NASH). Unfortunately, there are currently no approved drugs capable of effectively treating NASH due to the challenges in addressing fibrosis and restoring extracellular matrix (ECM) homeostasis. We discovered a significant up-regulation of interleukin-11 (IL-11) in fibrotic livers using two well-established murine models of NASH. To leverage this signaling pathway, we developed a nanoparticle (NP)-assisted RNA interfering approach that specifically targets activated HSCs (aHSCs), blocking IL-11/ERK signaling to regulate HSC transdifferentiation along with fibrotic remodeling. The most potent NP, designated NP-AEAA, showed enhanced accumulation in fibrotic livers with NASH and was primarily enriched in aHSCs. We further investigated the therapeutic efficacy of aHSC-targeting NP-AEAA encapsulating small interfering RNA (siRNA) against *IL11* or its cognate receptor *IL11ra1* (termed si*IL11*@NP-AEAA or si*IL11ra1*@NP-AEAA, respectively) for resolving fibrosis and NASH. Our results demonstrate that both si*IL11*@NP-AEAA and si*IL11ra1*@NP-AEAA effectively inhibit HSC activation and resolve fibrosis and inflammation in two well-established murine models of NASH. Notably, si*IL11ra1*@NP-AEAA exhibits a superior therapeutic effect over si*IL11*@NP-AEAA, in terms of reducing liver steatosis and fibrosis as well as recovering liver function. These results constitute a targeted nanoparticulate siRNA therapeutic approach against the IL-11 signaling pathway of aHSCs in the fibrotic liver, offering a promising therapeutic intervention for NASH and other diseases.

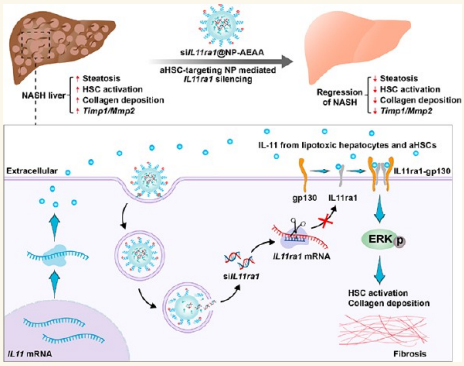

KEYWORDS: *activated HSC-targeted nanoparticles, targeted delivery of RNA-based therapeutics, nonalcoholic steatohepatitis, liver fibrosis, IL-11 signaling*

INTRODUCTION

With the rising prevalence of metabolic disorders such as obesity and diabetes, nonalcoholic steatohepatitis (NASH) is becoming a global public health crisis affecting approximately 5% of individuals worldwide.[1−3] NASH is characterized by hepatic lipid accumulation and inflammation, typically accompanied by pericellular fibrosis.[4,5] Progressive liver fibrosis in NASH is the main predictor of liver-related mortality,[6−8] and the clinical focus for NASH therapies has recently shifted towards mitigating fibrosis as a primary outcome measure.[9,10] It is widely accepted that the fibrogenic transformation of fibroblasts into myofibroblasts represents a key step in NASH pathogenesis.[11,12] This fibroblast-to-myofibroblast transformation is caused by the activation of hepatic stellate cells (HSCs).[13−15] The underlying mechanisms of HSC activation have been studied to inhibit the profibrogenic signaling in activated HSCs (aHSCs) to combat NASH and related fibrotic diseases, however, achieving therapeutic strategies with enhanced specificity and efficacy has perplexed researchers for many years, and currently there are no effective drugs approved for the treatment of liver fibrosis.[16−19]

Received: April 10, 2023
Accepted: July 21, 2023
Published: July 25, 2023

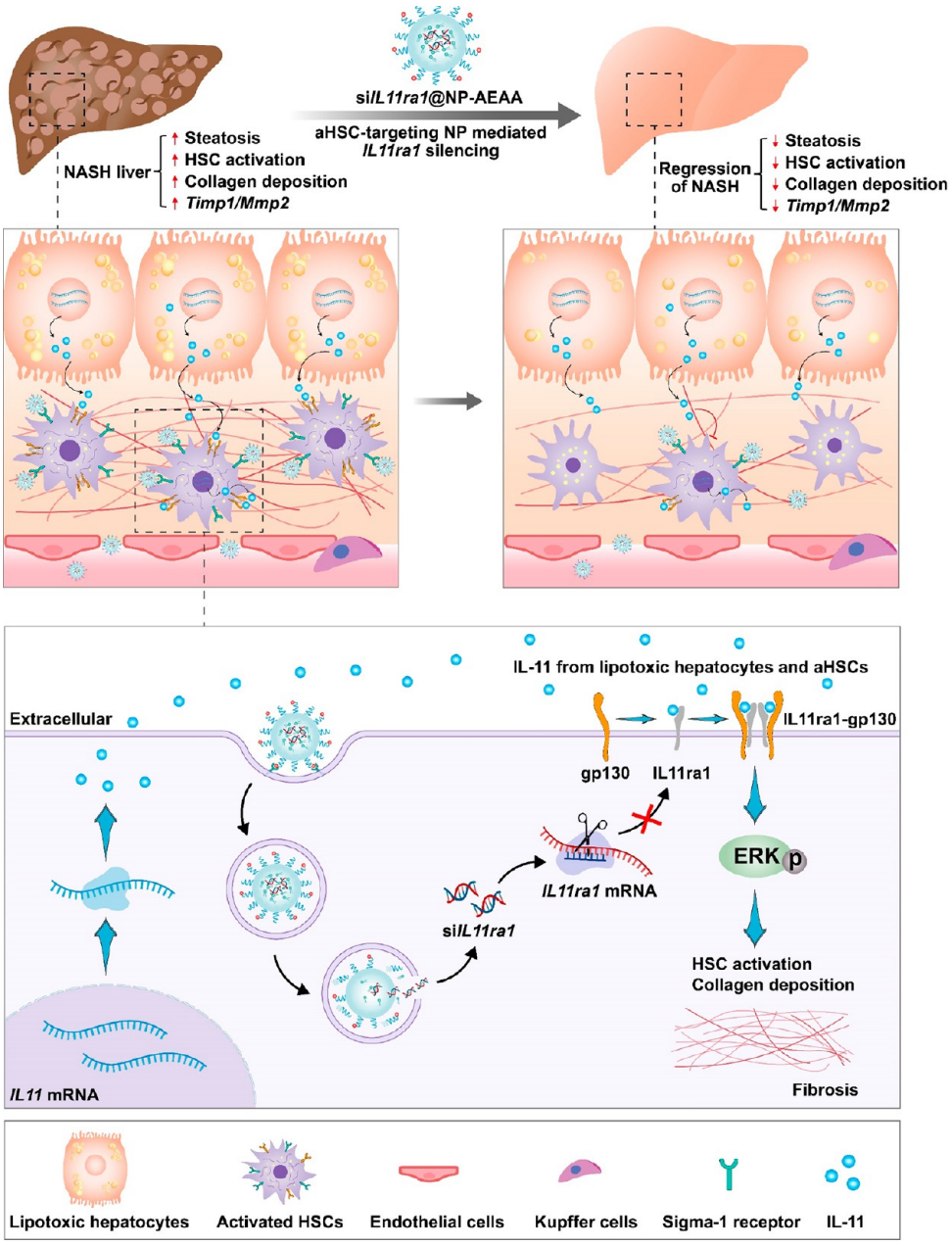

Figure 1. Schematic for delivery of si*IL11ra1*@NP-AEAA to aHSCs for the treatment of NASH and related fibrosis. The specially designed si*IL11ra1*@NP-AEAA accumulates in fibrotic livers and targets aHSCs residing in the space of Disse mediated by Sig-1R. Internalization of si*IL11ra1*@NP-AEAA allows the release of si*IL11ra1*, which effectively reduces the expression of IL11ra1 protein and inhibits the formation of the IL11ra1-gp130 complex, which in turn blocks HSC activation, reduces ECM deposition, and ameliorates inflammation via inhibition of noncanonical IL-11/ERK signaling and thereby encourages regression of NASH and related fibrosis in murine models of NASH.

Recent studies have confirmed that interleukin-11 (IL-11) is a vital profibrotic cytokine downstream of multiple stimuli that are involved in myofibroblast transdifferentiation and organ fibrosis.[20,21] Excess secreted IL-11 in NASH liver can bind with its cognate receptor (IL11ra1) and glycoprotein 130 (gp130) complex, driving HSC activation and noncanonical extracellular signal-regulated kinase (ERK)-dependent autocrine signaling responsible for pro-inflammatory and fibrogenic protein synthesis and subsequently, NASH progression.[22,23] Using both high-fat, high-cholesterol, methionine- and choline-deficient diet (HFCMCD)- and high-fat/high-cholesterol diet (HFHC)- induced murine models of NASH, we discovered a significant up-regulation of IL-11 and actin alpha 2, smooth muscle (ACTA2) in fibrotic livers (Figure S1A–C and Figure S2A–C). The strong correlation between IL-11 expression and ACTA2 which is a hallmark of HSC activation was identified by quantitative analysis of immunohistochemistry images (Figure S1D and Figure S2D), which is consistent with previous reports.[23,24] Western blotting also indicated that the increased expression of IL-11 and IL11ra1 in HSCs derived from both murine NASH models was closely associated with the activation of HSCs and elevated levels of ACTA2 (Figure S1E,F and Figure S2E,F), revealing the prominent roles IL-11 and IL11ra1 play in the pathogenesis of NASH. We therefore hypothesize that inhibiting IL-11 signaling by down-regulation

https://doi.org/10.1021/acsnano.3c03217
ACS Nano 2023, 17, 14852–14870

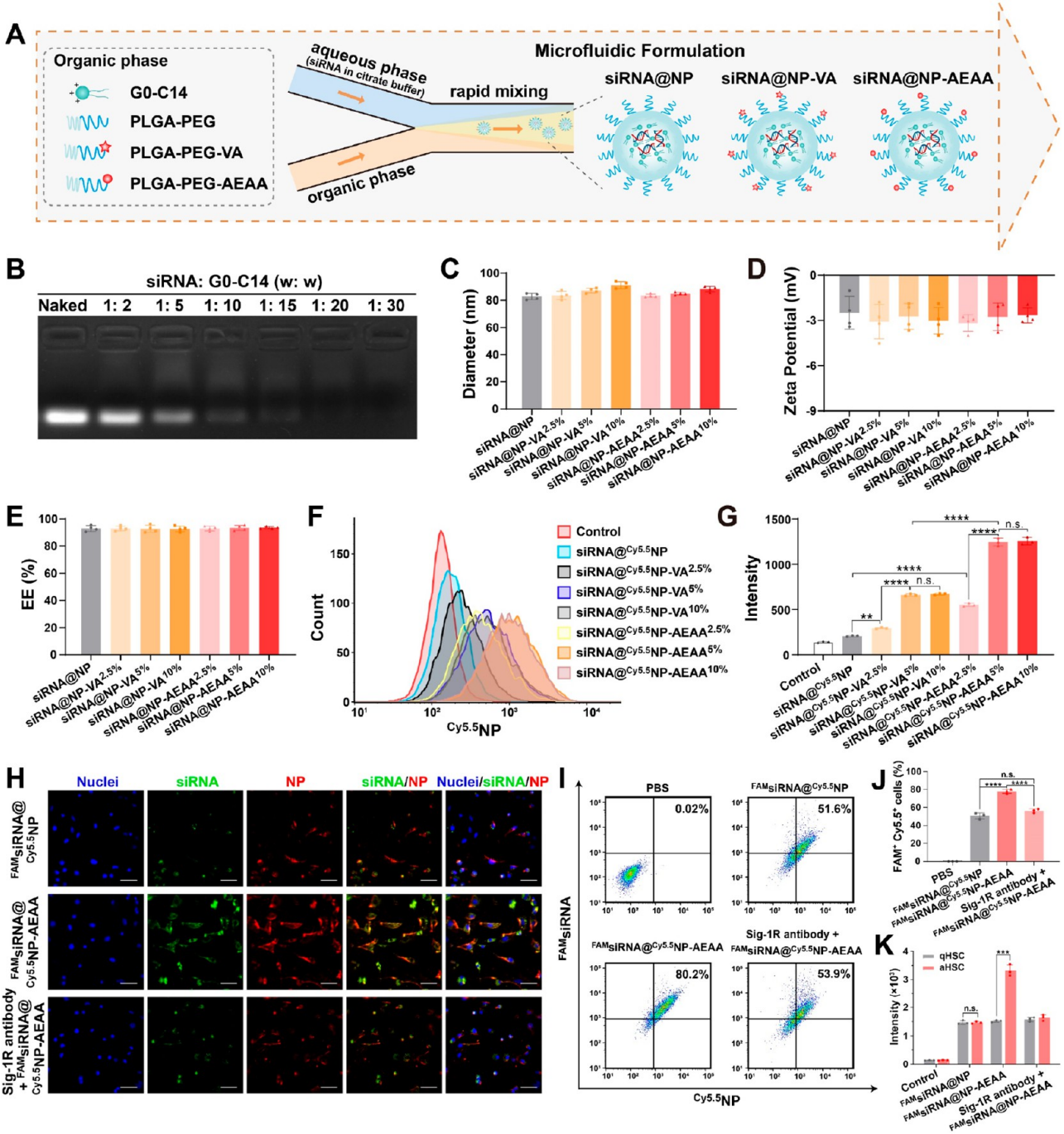

Figure 2. NP preparation, characterization, and cellular uptake. (A) NPs were prepared via a microfluidic method using PLGA-PEG-VA and PLGA-PEG-AEAA that were incorporated to impart stealth and targeting characteristics. (B) Electrophoretic mobility of siRNA in agarose gel. siRNA was complexed with G0-C14 at various weight ratios, and naked siRNA was used as a negative control. (C, D) Diameter (C) and zeta potential (D) of different siRNA-loaded NPs (n = 4). (E) siRNA encapsulation efficiency of different NPs (n = 4). (F, G) Flow cytometry histogram (F) and mean fluorescence intensity (G) of aHSCs treated with indicated NPs for 4 h (n = 3). (H–J) aHSCs were pretreated with/without Sig-1R antibody, followed by 4 h of incubation with indicated NPs, and NP uptake was evaluated by CLSM images (H) and flow cytometry analysis (I and J) (n = 3). NPs were labeled with Cy5.5 ($^{Cy5.5}$NP, red), siRNA was labeled with FAM (^{FAM}siRNA, green), and nuclei were stained with DAPI (blue). Scale bars represent 50 μm. (K) Mean fluorescence intensity of ^{FAM}siRNA in qHSCs and aHSCs that were pretreated with/without Sig-1R antibody followed by incubation with different NPs for 4 h, as indicated (n = 3). Statistical significance was determined via a two-tailed unpaired Student's t test (K) and a one-way ANOVA with post hoc Tukey test (G, J). Results are presented as means ± SD. $^{**}P < 0.01$, $^{***}P < 0.001$, $^{****}P < 0.0001$, n.s., not significant, $P > 0.05$.

of IL-11 or IL11ra1 in aHSCs can provide therapeutic benefits for NASH and related fibrosis.

RNA interference (RNAi) has emerged as a robust strategy for the treatment of many diseases.[25] To date, the majority of FDA-approved small interfering RNA (siRNA) therapeutics exclusively deliver siRNAs to parenchymal hepatocytes using an *N*-acetylgalactosamine (GalNAc)-based targeting strategy.[26] NP platforms that allow the specific delivery of therapeutic

https://doi.org/10.1021/acsnano.3c03217
ACS Nano 2023, 17, 14852–14870

siRNA to aHSCs for the treatment of NASH and related fibrosis have yet to be explored. Thus, there is an unmet demand to develop delivery vehicles capable of specifically transferring siRNA to cells other than liver hepatocytes to fully harness the potential of siRNA-based therapy for the treatment of liver diseases.

Herein, we present a targeted nanoparticle-mediated RNA therapeutic approach for the treatment of NASH and NASH-related liver fibrosis. Specifically, we demonstrate a proof-of-concept for the design and preclinical use of an aHSC-targeting NP-RNA interference approach against IL-11 signaling for the inhibition of hepatic fibrosis and amelioration of NASH (Figure 1). Our targeted nanoparticle therapeutics are composed of three components: (i) a cationic lipid-like molecule designated G0-C14 which facilitates siRNA entrapment and endosome escape following cellular internalization;[27] (ii) a biodegradable poly(lactide-*co*-glycolide)-*b*-poly(ethylene glycol) (PLGA-PEG) acting as a matrix protecting the encapsulated siRNA and prolonging the NP plasma circulation time; and (iii) a small molecule as targeting ligand to liver aHSCs (Figure 2A). Specifically, we chemically linked either vitamin A (VA), which specifically recognizes the retinol-binding protein (RBP) receptor, or aminoethyl anisamide (AEAA), which specifically recognizes the sigma-1 receptor (Sig-1R), at the free PEG end of PLGA-PEG to develop two different aHSC-targeting NPs. Using an HFCMCD-induced murine model of NASH, we showed that the NP designated NP-AEAA maximized accumulation in fibrotic NASH livers and was primarily enriched in aHSCs. We further investigated the efficacy of aHSC-targeting NP-AEAA encapsulating siRNA against either *IL11* or *IL11ra1* (termed si*IL11*@NP-AEAA or si*IL11ra1*@NP-AEAA, respectively) for ameliorating NASH and related hepatic fibrosis in both HFCMCD- and HFHC-induced murine models of NASH. Our results demonstrate that both si*IL11*@NP-AEAA and si*IL11ra1*@NP-AEAA effectively inhibit HSC activation and resolve fibrosis and inflammation by blocking the noncanonical IL-11/ERK signaling in the two well-established preclinical NASH models. si*IL11ra1*@NP-AEAA exhibits a superior therapeutic effect in terms of reducing liver steatosis and fibrosis, as well as recovering liver function when compared with si*IL11*@NP-AEAA. This work presents a targeting NP platform capable of delivering siRNA against IL-11 signaling to aHSCs, offering a promising therapeutic strategy for NASH patients suffering from fibrosis. Additionally, the developed NP-aided aHSC-targeting RNA therapeutic approach provides insights into the treatment of many other hepatic diseases.

RESULTS

Design, Synthesis, and Characterization of siRNA-Loaded NPs for aHSC-Specific Targeting. It has been reported that the liver usually captures up to 90% of administered NPs from blood circulation due to its biological filtration function.[28] This intrinsic characteristic can be leveraged to endow NPs with the capability to target hepatic diseases. However, most of the captured NPs are preferentially taken up and sequestered by liver-resident Kupffer cells, followed by elimination through the hepatobiliary system,[29] resulting in limited NP delivery to the targeted diseased cells. Developing delivery strategies capable of specifically transferring nucleic acid-based therapeutics to certain types of liver cells is critically needed to enable the use of NPs for treating hepatic diseases. Using a microfluidic method, we fabricated engineered NPs through self-assembly of G0-C14 together with targeting polymeric excipients for selective delivery of RNA into nonparenchymal aHSCs in the fibrotic liver. G0-C14 was synthesized by reacting poly(amidoamine) (PAMAM) dendrimer generation 0 with 1,2-epoxytetradecane as described in Figure S3. The chemical structure of G0-C14 was characterized by ^{1}H nuclear magnetic resonance (^{1}H NMR, 400 MHz, Chloroform-*d*) as shown in Figure S4. To facilitate the active transport of siRNA-loaded NPs to aHSCs, we synthesized VA- and AEAA-functionalized PLGA-PEG as two different targeting polymeric excipients. VA in blood circulation can be specifically taken up by HSCs via RBP receptors.[30] This intrinsic attribute makes VA an attractive ligand for achieving the selective delivery of a drug to HSCs. AEAA is a benzamide-based compound that has a high affinity for the Sig-1R overexpressed on aHSCs in the metastatic liver.[31] We synthesized PLGA-PEG-VA by coupling VA to the carboxy end-group of PLGA-PEG-COOH as shown in Figures S5 and S6. We measured the UV absorbance at 328 nm as an indicator of the chemical composition of VA in the PLGA-PEG-VA conjugate. The amount of VA attached to the polymer conjugate was calculated as 0.62% w/w, corresponding to 0.95 molar VA per molar of PLGA-PEG-VA. Figure S7 demonstrates the synthetic route we used to synthesize PLGA-PEG-AEAA. ^{1}H NMR characteristic signals of aryl of AEAA (7.40 and 7.16 ppm) and methine of PLGA (5.28−5.05 ppm) were used to determine the chemical composition of AEAA in PLGA-PEG-AEAA. The result revealed that 0.97 molar AEAA was covalently attached to per molar of the polymer conjugate.

The siRNA complexation ability of G0-C14 was determined by an agarose gel electrophoresis assay. As shown in Figure 2B, siRNA could be successfully retarded by G0-C14 at a siRNA/G0-C14 weight ratio of 1:20. This ratio was chosen to form siRNA-loaded NPs in the following studies. We then formulated siRNA-loaded NPs with different weight ratios of PLGA-PEG-VA or PLGA-PEG-AEAA (2.5%, 5%, and 10% w/w the total polymeric excipients) and evaluated their key physicochemical attributes. No notable changes in particle size were observed for NPs prepared with 2.5% and 5% w/w of targeting polymeric excipients, while particle size slightly increased from 82.80 ± 2.09 nm (siRNA@NP) to 91.25 ± 2.27 nm (siRNA@NP-VA$^{10\%}$) and 88.33 ± 1.71 nm (siRNA@NP-AEAA$^{10\%}$) when 10% w/w PLGA-PEG was replaced with targeting polymeric excipients (Figure 2C). All NPs showed similar zeta potential in PBS solution (pH = 7.4) and siRNA encapsulation efficiency (EE) of around 93% (Figure 2D,E and Table S1).

Primary HSCs isolated from C57BL/6J mice were stimulated with transforming growth factor-β1 (TGF-β1) to induce their transformation into aHSCs, with the percentage of ACTA2-positive (ACTA2^{+}) cells surpassing 98%. Cellular internalization of different Cy5.5-labeled NPs ($^{Cy5.5}$NPs) was evaluated in the cultured aHSCs. Flow cytometry analysis exhibited that NP uptake by aHSCs increased with an increase in the weight ratio of the incorporated targeting moiety and reached a plateau when NPs were formulated with the PLGA-PEG-ligand at a weight ratio of 5% or above (Figure 2F,G). We noted that aHSCs treated with siRNA@NP-AEAA$^{5\%}$ showed the highest Cy5.5 fluorescence intensity, which was 1.89-fold higher than that of siRNA@NP-VA$^{5\%}$ and 6.05-fold higher than that of siRNA@$^{Cy5.5}$NP. Confocal laser scanning microscopy (CLSM) images of $^{Cy5.5}$NP-AEAA$^{5\%}$ loaded with FAM-labeled siRNA (termed ^{FAM}siRNA@$^{Cy5.5}$NP-AEAA)

https://doi.org/10.1021/acsnano.3c03217
ACS Nano 2023, 17, 14852−14870

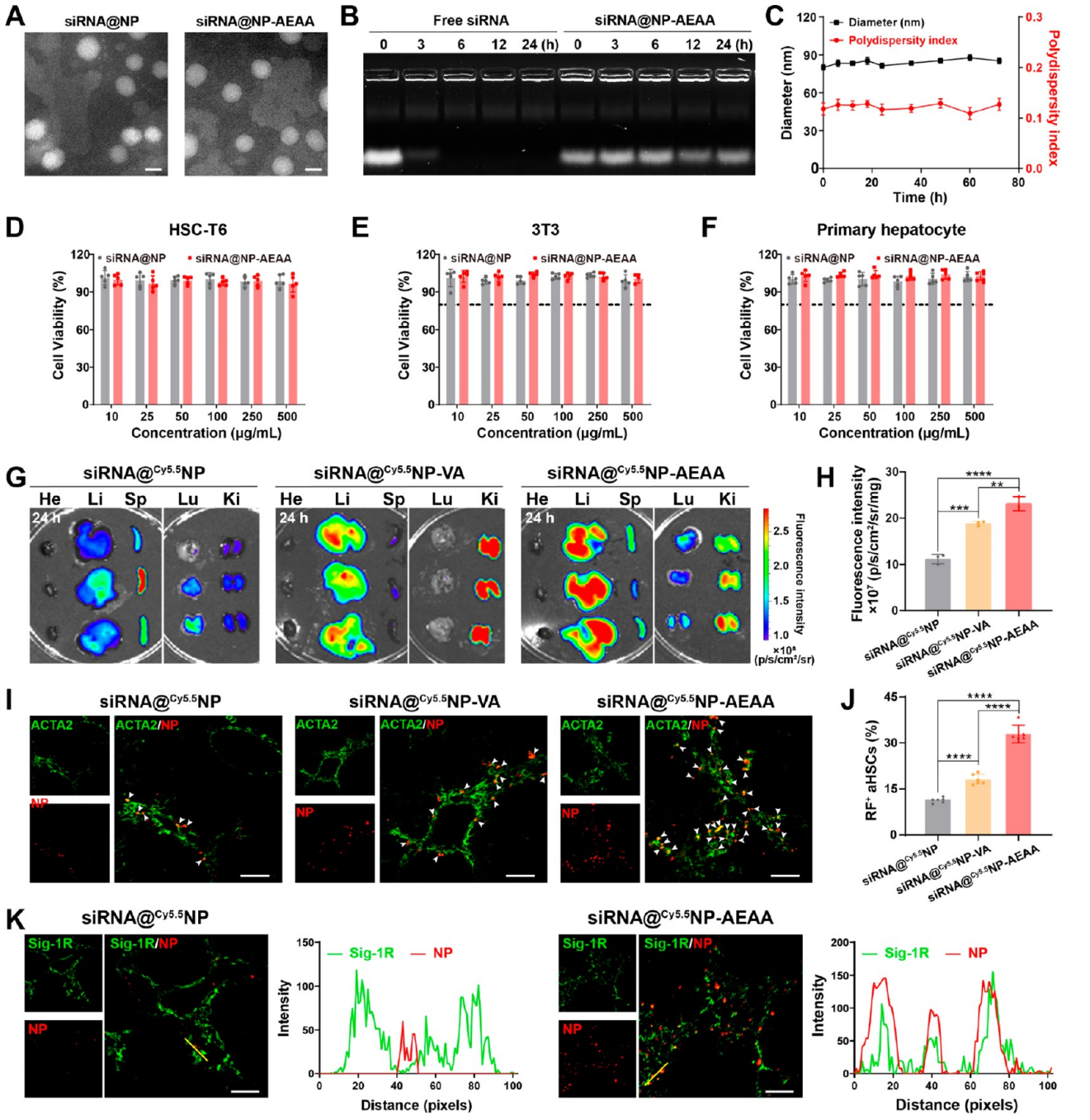

Figure 3. NP-AEAA characterization and in vivo biodistribution. (A) Representative TEM images of siRNA@NP and siRNA@NP-AEAA. Scale bars represent 50 nm. (B) Stability of free siRNA and NP-AEAA-encapsulating siRNA against serum at various time points. (C) The size and PDI of siRNA@NP-AEAA were monitored by dynamic light scattering (DLS) for 72 h (n = 3). (D−F) CCK8 assay of siRNA@NP and siRNA@NP-AEAA in HSC-T6 (D), 3T3 (E) and primary hepatocytes (F) (n = 5). (G) IVIS imaging of heart (He), liver (Li), spleen (Sp), lung (Lu), and kidneys (Ki) collected at 24 h from HFCMCD-fed mice following intravenous injection with indicated NPs. (H) Quantification analysis of the Cy5.5 fluorescence signal in HFCMCD mouse livers by Living Image 4.5 software (n = 3). (I) Immunofluorescence analysis of the colocalization of Cy5.5-labeled NPs (red) and ACTA2$^+$ aHSCs (green, Cora594-labeled) in liver sections from HFCMCD-induced fibrotic mice. Scale bars are 100 μm. White arrowheads indicate the colocalization of NPs with ACTA2. (J) Impact of targeting ligands on in vivo cellular uptake of Cy5.5-labeled (RF$^+$) NPs by ACTA2$^+$ aHSCs. Three mice were measured for each group, and two randomly selected liver sections of each mouse were analyzed by ImageJ, resulting in a total of six measurements. (K) Intracellular distribution of NPs in fibrotic liver sections from HFCMCD mice receiving siRNA@$^{Cy5.5}$NP or siRNA@$^{Cy5.5}$NP-AEAA. The fluorescence intensity profiles were measured along the yellow line drawn across representative areas. Sig-1R was visualized by Cora594 (green), and NPs were labeled with Cy5.5 (red). Scale bars represent 100 μm. Statistical significance was determined via a one-way ANOVA with post hoc Tukey test (H, J). Results are presented as means ± SD. $^{**}P < 0.01$, $^{***}P < 0.001$, $^{****}P < 0.0001$.

further confirmed that incorporation of 5% w/w AEAA resulted in more siRNA and NPs colocalized within aHSCs (Figure 2H). Notably, cellular uptake of ^{FAM}siRNA@$^{Cy5.5}$NP-AEAA by aHSCs was substantially inhibited in the presence of

https://doi.org/10.1021/acsnano.3c03217
ACS Nano 2023, 17, 14852−14870

the Sig-1R antibody, which is likely a result of the blockage of Sig-1R (Figure 2H). Flow cytometry analysis shows similar results (Figure 2I,J). Compared with nontargeted ^{FAM}siRNA@$^{Cy5.5}$NP, ^{FAM}siRNA@$^{Cy5.5}$NP-AEAA treatment resulted in a significantly higher percentage of aHSCs positively stained with both FAM and Cy5.5; this percentage markedly decreased from 80.6% to 56.3% when cells were pretreated with Sig-1R antibody, thus indicating Sig-1R-mediated endocytosis. It is noteworthy that the enhancement in NP uptake observed in NP-AEAA-treated aHSCs was not observed in quiescent HSCs (qHSCs) that do not express Sig-1R (Figure 2K and Figure S9). FAM fluorescence intensity in aHSCs treated with ^{FAM}siRNA@NP-AEAA was 2.18-fold higher than that in qHSCs treated with the same targeted NPs (Figure 2K). As expected, the enhanced fluorescence intensity observed in ^{FAM}siRNA@NP-AEAA-treated aHSCs was dramatically reduced by Sig-1R antibody treatment, indicating that the aHSC-specific uptake of NP-AEAA is mainly mediated via the AEAA-Sig-1R interaction.

siRNA@NP-AEAA Characterization and In Vivo Targeting Evaluation. We characterized the morphologies of siRNA@NP and siRNA@NP-AEAA using transmission electron microscopy (TEM). As shown in Figure 3A, both NPs showed a spherical and uniform structure, revealing that the incorporation of targeting moieties has no obvious effect on NP morphology. We then performed gel electrophoresis to examine whether the developed NP-AEAA could protect siRNA from serum nuclease degradation. Figure 3B shows that naked siRNA was rapidly degraded in PBS supplemented with 20% fetal bovine serum (FBS), while siRNA extracted from NP-AEAA remained intact after 24 h of incubation, indicating an increase in stability of NP-formulated siRNA. Additionally, no significant change in NP size or polydispersity index (PDI) was observed after 72 h of incubation of siRNA@NP-AEAA with PBS (pH = 7.4) containing 20% FBS at 37 °C (Figure 3C). Cytotoxicity of siRNA@NP and siRNA@NP-AEAA was assessed in the rat liver stellate cell line HSC-T6, mouse fibroblast cell line NIH/3T3, and mouse primary hepatocytes using cell counting kit-8 (CCK8) assay. The results showed no cytotoxicity in the range of tested concentrations, and the viability of the three cells remained above 90% at a high NP concentration up to 500 μg/mL (Figure 3D−F).

The superior targeting efficacy of NP-AEAA in vitro prompted us to investigate whether NP-AEAA could be specifically delivered to aHSCs in HFCMCD-induced fibrotic mice. C57BL/6J mice were fed the HFCMCD diet for 12 weeks to induce hepatic lesion characteristics of NASH, with steatosis, lobular inflammation, and severe fibrosis (Figure S10). An IVIS imaging system was used to examine the biodistribution of different NPs in vivo following intravenous injection. As shown in Figure 3G,H, intravenously injected siRNA@$^{Cy5.5}$NP-VA$^{5\%}$ and siRNA@$^{Cy5.5}$NP-AEAA$^{5\%}$ exhibited greater accumulation in fibrotic livers compared with nontargeted siRNA@$^{Cy5.5}$NP, and siRNA@$^{Cy5.5}$NP-AEAA$^{5\%}$ resulted in the highest Cy5.5 fluorescence intensity in liver tissues. It is expected to observe NP accumulation in the liver and spleen due to the sinusoidal endothelial capillaries in the liver and a large population of macrophages in the spleen.[32,33] As the kidney is the major organ responsible for drug elimination, NP accumulation is also expected in this organ (Figure S11).[34] Immunofluorescence staining of liver sections indicated that $^{Cy5.5}$NP-AEAA primarily colocalized within aHSCs positively stained for ACTA2 (the most reliable aHSC marker), generating bright yellow signals (Figure 3I). The quantitative analysis of imaging illustrated that the percentage of Cy5.5 red fluorescence-positive (RF$^+$) cells accounted for 32.9 ± 2.9% of the total area of ACTA2$^+$ aHSCs in liver sections obtained from mice receiving $^{Cy5.5}$NP-AEAA, which was higher than those of $^{Cy5.5}$NP-VA (18.1 ± 1.7%) and nontargeted $^{Cy5.5}$NP treatment groups (11.5 ± 0.8%) (Figure 3J). Intriguingly, $^{Cy5.5}$NP-AEAA-mediated enhanced NP accumulation in fibrotic livers of HFCMCD mice was not observed in healthy mouse livers, where ACTA2$^+$ aHSCs were hardly detected (Figures S12 and S13). This is presumably due to the limited uptake of NP-AEAA by qHSCs in the livers of normal chow-fed healthy mice. Consistent with in vitro results, the in vivo results further demonstrate that incorporation of AEAA facilitates NP accumulation within fibrotic livers more efficiently than VA, and injected NP-AEAA is preferentially localized within aHSCs.

To validate the HSC-specific targeting ability of NP-AEAA, we collected hepatocytes and HSCs from HFCMCD mice receiving treatment of siRNA@$^{Cy5.5}$NP or siRNA@$^{Cy5.5}$NP-AEAA and conducted flow cytometry analysis. The results showed that the targeted siRNA@$^{Cy5.5}$NP-AEAA achieved 8.5-fold higher percentage of Cy5.5-positive (Cy5.5$^+$) HSCs compared with its nontargeted counterpart siRNA@$^{Cy5.5}$NP, but both NPs showed similar delivery to parenchymal hepatocytes (Figure S14A−C). The ratio of Cy5.5$^+$ cells between HSCs and hepatocytes (Cy5.5$^+$ HSCs/Cy5.5$^+$ hepatocytes, an indicator of HSC selectivity) was calculated to be 1.73 for siRNA@$^{Cy5.5}$NP-AEAA, with 41.5% of the total HSCs displaying Cy5.5 positive cells and 24.0% hepatocytes colocalized with NPs (Figure S14C). In contrast, only a small ratio of 0.21 was observed for siRNA@$^{Cy5.5}$NP. It has been reported that HSCs are difficult to transfect and take up foreign materials in comparation with hepatocytes, a ratio of Cy5.5$^+$ HSCs/Cy5.5$^+$ hepatocytes below 1 is expected.[35] Notably, our developed siRNA@$^{Cy5.5}$NP-AEAA achieves a 1.73-fold higher ratio, indicating the dramatically increased preferential uptake of NPs by HSCs over hepatocytes in vivo.

To investigate whether the in vivo uptake of NP-AEAA by aHSCs is mediated by Sig-1R, we examined the expression and colocalization of Sig-1R in liver tissues. Figure S15 showed markedly elevated expression of Sig-1R in the HFCMCD-induced fibrotic liver compared with the healthy control, and colocalization of Sig-1R with ACTA2$^+$ aHSCs, suggesting that aHSCs express high levels of Sig-1R. Additionally, we observed robust expression of Sig-1R and strong Cy5.5 fluorescence signal of NPs in fibrotic livers of HFCMCD mice receiving siRNA@$^{Cy5.5}$NP-AEAA (Figure 3K). The line scanning profiles toward the selected cells demonstrated that the red Cy5.5 signal from NPs primarily overlapped with the green Sig-1R signal. In contrast, treatment with nontargeted siRNA@$^{Cy5.5}$NP resulted in much less NP accumulation in fibrotic liver sections as well as minimal colocalization of the red NP signal with the green Sig-1R. On the other hand, reduced Sig-1R expression was observed in liver sections obtained from healthy mice receiving NP-AEAA, leading to limited NP accumulation (Figure S16), which is consistent with the data shown in Figure S12. Taken together, these results reveal that homing of NP-AEAA to aHSCs is mediated by the interaction of AEAA and Sig-1R that is expressed on aHSCs.

***siIL11*@NP-AEAA and *siIL11ra1*@NP-AEAA Both Inhibit HSC Activation, Migration, and Invasion through ERK Signaling Blockade.** We next studied the effect of IL-11

https://doi.org/10.1021/acsnano.3c03217
ACS Nano 2023, 17, 14852−14870

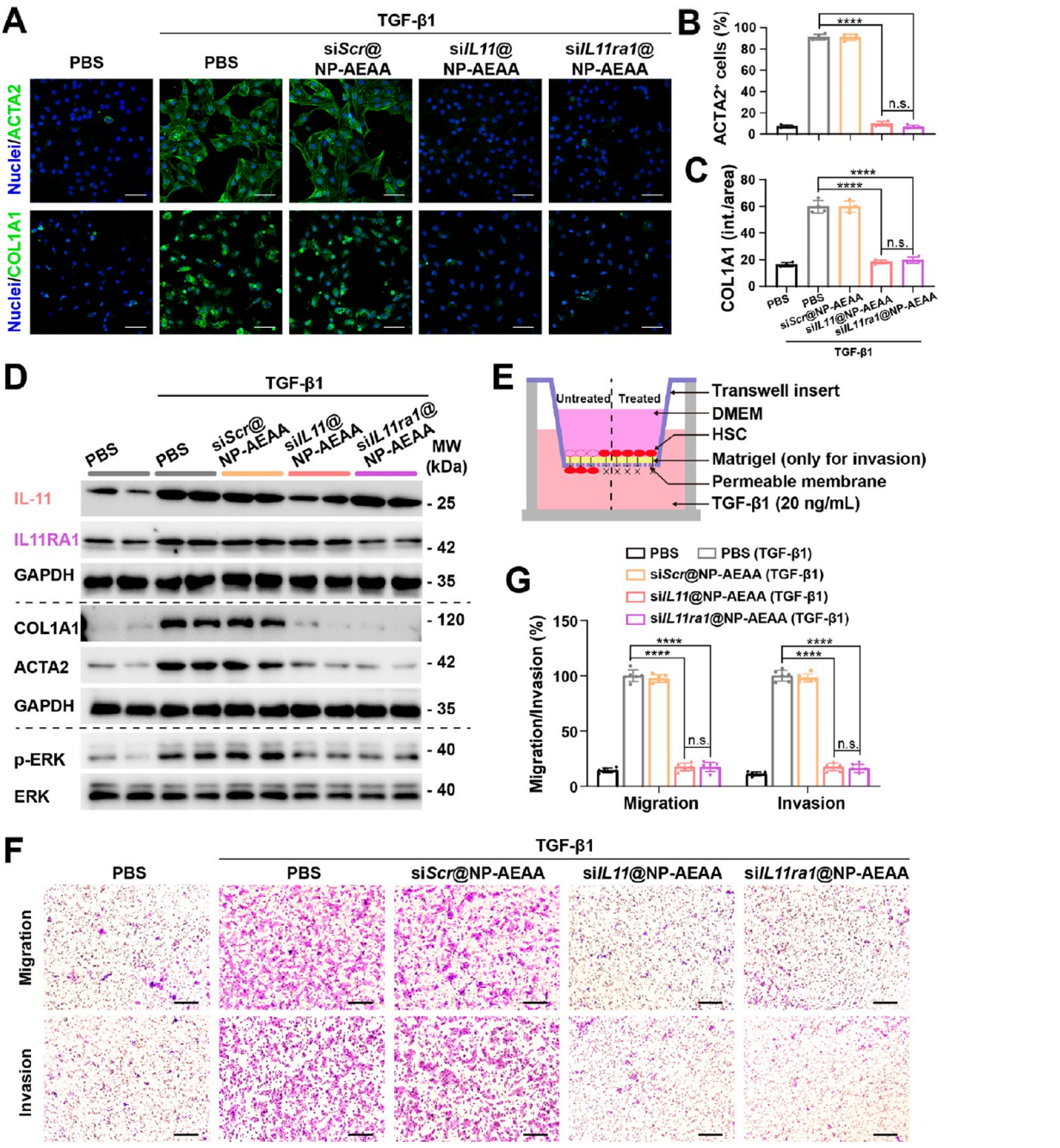

Figure 4. Suppression of IL-11 or IL11RA1 using NP-AEAA siRNA therapeutics inhibits the activation, migration, and invasion of HSCs in vitro. (A) Representative images of ACTA2 and COL1A1 immunostaining in HSCs treated with TGF-β1 (20 ng/mL) for 48 h in the presence of PBS, si*Scr*@NP-AEAA, si*IL11*@NP-AEAA, or si*IL11ra1*@NP-AEAA. HSCs treated with PBS and without any stimulation served as the "basal" state. Scale bars represent 50 μm. (B, C) Quantification analysis of ACTA2$^+$ cells (B) and COL1A1 immunofluorescence intensity (C) in HSCs as shown in Figure 4A. n = 4. (D) Western blots of IL-11, IL11RA1, COL1A1, ACTA2, phosphorylation, and total expression of ERK in HSCs treated with PBS, si*Scr*@NP-AEAA, si*IL11*@NP-AEAA, or si*IL11ra1*@NP-AEAA followed by TGF-β1 stimulation (20 ng/mL) for 48 h. n = 2 samples per group. GAPDH was used as a loading control to normalize protein levels, with HSCs treated with PBS alone serving as a negative control. MW, molecular weight. (E) Schematic illustration of the HSC migration and invasion assay using a two-compartment Boyden chamber system. Cells were incubated with PBS, si*Scr*@NP-AEAA, si*IL11*@NP-AEAA, or si*IL11ra1*@NP-AEAA in the top chamber, and the medium in the bottom chamber was supplemented with chemotactic stimuli. For the invasion assay, the upper side of the polycarbonate membrane in the upper chamber was coated with a Matrigel matrix enriched with type IV collagen. HSCs migrate and invade through the membrane into the bottom chamber. (F, G) Microscopy images (F) and quantitative analysis (G) of stained HSCs that invaded through the Matrigel matrix and migrated from the top chamber to the bottom chamber in response to TGF-β1 stimulation (20 ng/mL) following the indicated treatments (n = 3). Images from two randomly selected fields per well were acquired, and three independent wells were measured, resulting in a total of six measurements. Migration (%) or invasion (%) was expressed as a percentage of NP-treated cells passing through the membrane relative to the number of PBS-treated cells that traversed the membrane following stimulation with TGF-β1. Scale bars represent 100 μm. Statistical significance was determined via a one-way ANOVA with Tukey test (B, C, and G). Results are presented as means $\pm$ SD. ****P < 0.0001, n.s., not significant, P > 0.05.

https://doi.org/10.1021/acsnano.3c03217
ACS Nano 2023, 17, 14852−14870

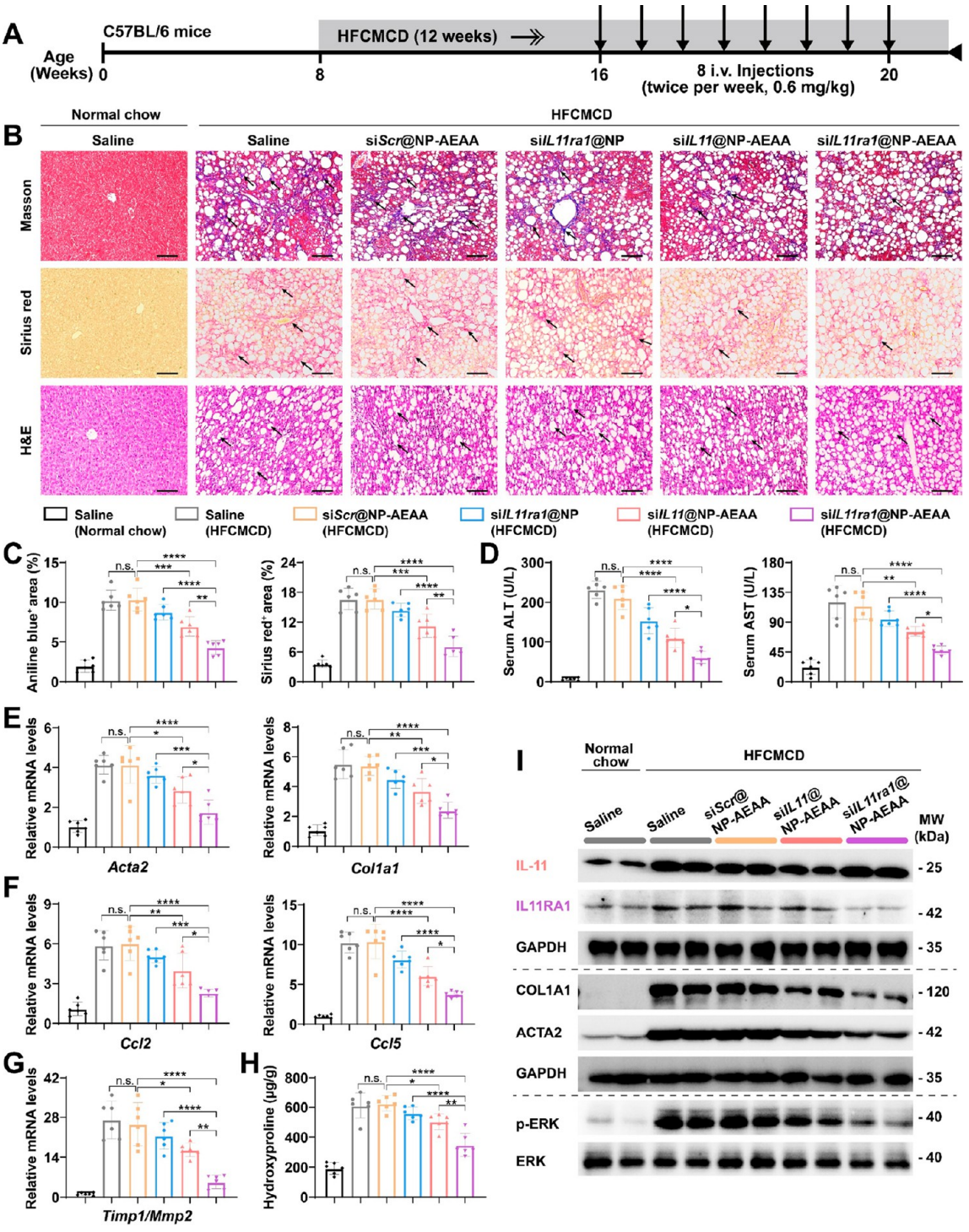

Figure 5. si*IL11ra1*@NP-AEAA shows superior efficacy on hepatic fibrosis and inflammation in an HFCMCD-induced NASH model. (A) Schematic diagram of the HFCMCD-induced NASH model and treatment timeline for saline, si*Scr*@NP-AEAA, si*IL11ra1*@NP, si*IL11*@NP-AEAA, or si*IL11ra1*@NP-AEAA therapy. (B) Representative microscopic images of Masson's trichrome staining (collagen fibers are stained blue; muscle tissue is stained red), Sirius red staining (collagen I and III fibers are red) and H&E staining (black arrows indicate macrovesicular steatosis) of liver tissue sections obtained from normal chow-fed healthy mice, or HFCMCD-fed mice treated with indicated NPs. Scale bars represent 100 μm. (C) Quantification analysis of aniline blue- and Sirius red-positive areas in liver sections. n = 6 mice per group. (D) Serum ALT and AST levels of mice receiving the indicated treatments. n = 6 mice per group. (E, F) Hepatic mRNA expression of profibrogenic (*Acta2*, *Col1a1*) (E) and proinflammatory (*Ccl2*, *Ccl5*) genes (F) following indicated treatments. n = 6 mice per group. (G) Relative mRNA expression of *Timp1/Mmp2* in livers of HFCMCD mice receiving the indicated treatments. n = 6 mice per group. (H) Quantification analysis of liver hydroxyproline content. n = 6 mice per group. (I) Western blots of IL-11, IL11RA1, COL1A1, ACTA2, phosphorylation, and total expression of ERK in the livers collected from the indicated groups. n = 2 mice per group. GAPDH was used as a loading control to normalize the protein levels. Statistical significance was determined via a one-way ANOVA with a post hoc Tukey test (C−H). Results are presented as means ± SD. *P < 0.05, **P < 0.01, ***P < 0.001, ****P < 0.0001, n.s., not significant, P > 0.05.

https://doi.org/10.1021/acsnano.3c03217
ACS Nano 2023, 17, 14852−14870

signaling on the activation of HSCs. Our data showed that stimulation with NASH stimuli, including TGF-β1, basic fibroblast growth factor (bFGF), platelet-derived growth factor (PDGF) and oxidative stress (H_2O_2), led to IL-11 secretion from primary HSCs and a marked increase in the proportion of $ACTA2^+$ cells (Figure S17). These findings imply that IL-11 is a downstream effector of multiple NASH stimuli and is responsible for the HSC-to-myofibroblast transformation. We then treated TGF-β1-stimulated HSCs with si*IL11*- or si*IL11ra1*-encapsulated NP-AEAA (termed si*IL11*@NP-AEAA or si*IL11ra1*@NP-AEAA, respectively). Immunofluorescence staining revealed that both treatments effectively inhibited the elevated expression of ACTA2 and collagen type I alpha 1 (COL1A1, the main components of the ECM) induced by TGF-β1 and other stimulation factors, such as bFGF, PDGF and H_2O_2 (Figure 4A−C and Figure S18). Western blotting results further confirmed a reduction in the expression of IL-11 and IL11RA1 upon treating TGF-β1-stimulated HSCs with si*IL11*@NP-AEAA and si*IL11ra1*@NP-AEAA, respectively, resulting in a noticeable decrease in the level of TGF-β1-induced expression of ACTA2 and COL1A1 (Figure 4D and Figure S19). It is believed that IL-11-driven noncanonical ERK phosphorylation is associated with HSC activation and NASH pathologies.[23] Figure 4D and Figure S19 show that treatment with si*IL11*@NP-AEAA or si*IL11ra1*@NP-AEAA abolished TGF-β1-induced phosphorylated ERK (p-ERK) expression in HSCs, suggesting that the developed siRNA therapeutics effectively inhibit HSC activation and ECM production by blocking IL-11-dependent ERK signaling.

The basement membrane-like matrix present within the space of Disse provides a residential microenvironment for HSCs.[36] During liver fibrosis and NASH pathologies, this basement membrane-like matrix gradually transitions to a fibrillar matrix and is accompanied by the release of profibrogenic growth factors such as TGF-β1 from aHSCs, inflammatory cells, and hepatocytes.[37,38] Stimulation with profibrogenic growth factors further activates HSCs, prompting them to invade adjacent areas and migrate toward injured areas of the Disse space, thus contributing to the spread and progression of the disease.[39] Here we examined the effect of si*IL11*@NP-AEAA and si*IL11ra1*@NP-AEAA on the stimuli-induced migration of HSCs via a classical two-compartment Boyden chamber system. Figure 4E presents a schematic illustration of the experimental design. Cells were incubated on the upper side of the polycarbonate membrane in the upper chamber, which represents the normal space of the Disse microenvironment. Figure 4F demonstrates that only a few cells migrated through the pores of the membrane without chemotactic stimuli from the lower chamber. When the medium in the lower chamber was supplemented with TGF-β1 to simulate the inflamed Disse microenvironment, aHSCs treated with si*Scr*@NP-AEAA or PBS controls exhibited a significantly increased rate of migration. Intriguingly, si*IL11*@NP-AEAA and si*IL11ra1*@NP-AEAA treatments significantly decreased the migratory rate of TGF-β1-stimulated HSCs to 16.62% and 16.71%, respectively, compared with si*Scr*@NP-AEAA and PBS controls (Figure 4F,G). To study the impact of targeted NP-assisted siRNA therapeutics on the invasion of HSCs activated by TGF-β1, Matrigel enriched with type IV collagen was used to coat the upper side of the polycarbonate membrane in the upper chamber, simulating the ECM and providing an anchor for resident HSCs. Similarly, treatments with si*IL11*@NP-AEAA and si*IL11ra1*@NP-AEAA significantly reduced the invasion rate of TGF-β1-stimulated HSCs to 15.37% and 13.52%, respectively, compared to si*Scr*@NP-AEAA and PBS controls (Figure 4F,G). These data reveal the pivotal role of IL-11 in HSC migration and invasion and suggest that effective suppression of IL-11 or IL11ra1 through NP-AEAA-assisted siRNA therapeutics could anchor HSCs and prevent them from dispersing in the Disse space and from migrating to sites of injury in the liver, thereby inhibiting the progression of liver fibrosis.

si*IL11ra1*@NP-AEAA Ameliorates Fibrosis and Inflammation in an HFCMCD-Induced NASH Model. In preliminary studies, we investigated the antifibrotic effect of si*IL11ra1*@NP-AEAA at a high dose (0.6 mg/kg of si*IL11ra1*) and a low dose (0.3 mg/kg of si*IL11ra1*) in an HFCMCD-induced NASH model (Figure S20A). The results showed that treatments with both high and low doses of si*IL11ra1* decreased the liver damage markers of ALT and AST, with a high dose of si*IL11ra1*@NP-AEAA treatment having a more pronounced effect than low dose treatment (Figure S20B,C). HFCMCD mice receiving si*IL11ra1*@NP-AEAA treatment at a high dose showed substantially reduced hydroxyproline content in liver homogenates and Sirius red-stained fibrotic area in liver tissues compared with the low-dose treatment (Figure S20D−F). Additionally, we tested the silencing activity of si*IL11ra1*@NP-AEAA at different doses in HSCs isolated from HFCMCD-induced mice. Western blotting results showed that there was a dose-dependent silencing activity of si*IL11ra1*@NP-AEAA and ∼63.7% knockdown of IL11RA1 could be achieved at a dose of 0.6 mg/kg (Figure S20G,H), indicating a positive correlation between antifibrotic effects and down-regulation of IL11RA1 in HSCs. Taken together, we selected a dose of 0.6 mg siRNA per kg for the following in vivo experiments. Figure 5A illustrates the therapeutic efficacy of aHSC-homing siRNA therapeutics that target the IL-11 signaling in the HFCMCD-induced NASH model. Masson's trichrome and Sirius red staining, followed by quantitative analysis, revealed that the fibrotic regions were markedly increased in the livers of HFCMCD mice treated with saline or si*Scr*@NP-AEAA in comparison with those of normal chow-fed healthy mice (Figure 5B,C). NP-mediated silencing of *IL-11* or *IL11ra1* decreased the aniline blue- or Sirius red-positive area in liver tissues, with targeted NP-AEAA-mediated siRNA therapeutics having a more pronounced effect than non-targeted NP. Specifically, HFCMCD mice receiving si*IL11-ra1*@NP-AEAA treatment demonstrated the fewest fibrotic regions among groups (Figure 5B,C). Serological analysis revealed that the HFCMCD diet induced a significant liver injury, as evidenced by increased serum levels of alanine transaminase (ALT) and aspartate transaminase (AST). Although nontargeted si*IL11ra1*@NP treatment mitigated liver damage compared with HFCMCD controls, targeted si*IL11ra1*@NP-AEAA treatment reduced both enzymes to near normal ranges (Figure 5D).

Differentiation of HSCs into myofibroblast-like aHSCs is a key step involved in the progression of NASH and fibrosis, which leads to elevated expression of ACTA2 and promotes the production of COL1A1 and proinflammatory chemokines C−C motif chemokine ligands 2 (CCL2) and CCL5.[40,41] Quantitative real-time polymerase chain reaction (qRT-PCR) analysis of liver homogenates indicated that blockage of the IL-11 signaling pathway mediated by NPs markedly down-regulated the elevated expression levels of *Acta2*, *Col1a1*, *Ccl2*, and *Ccl5* induced by the HFCMCD diet. Among the test

https://doi.org/10.1021/acsnano.3c03217
ACS Nano 2023, 17, 14852−14870

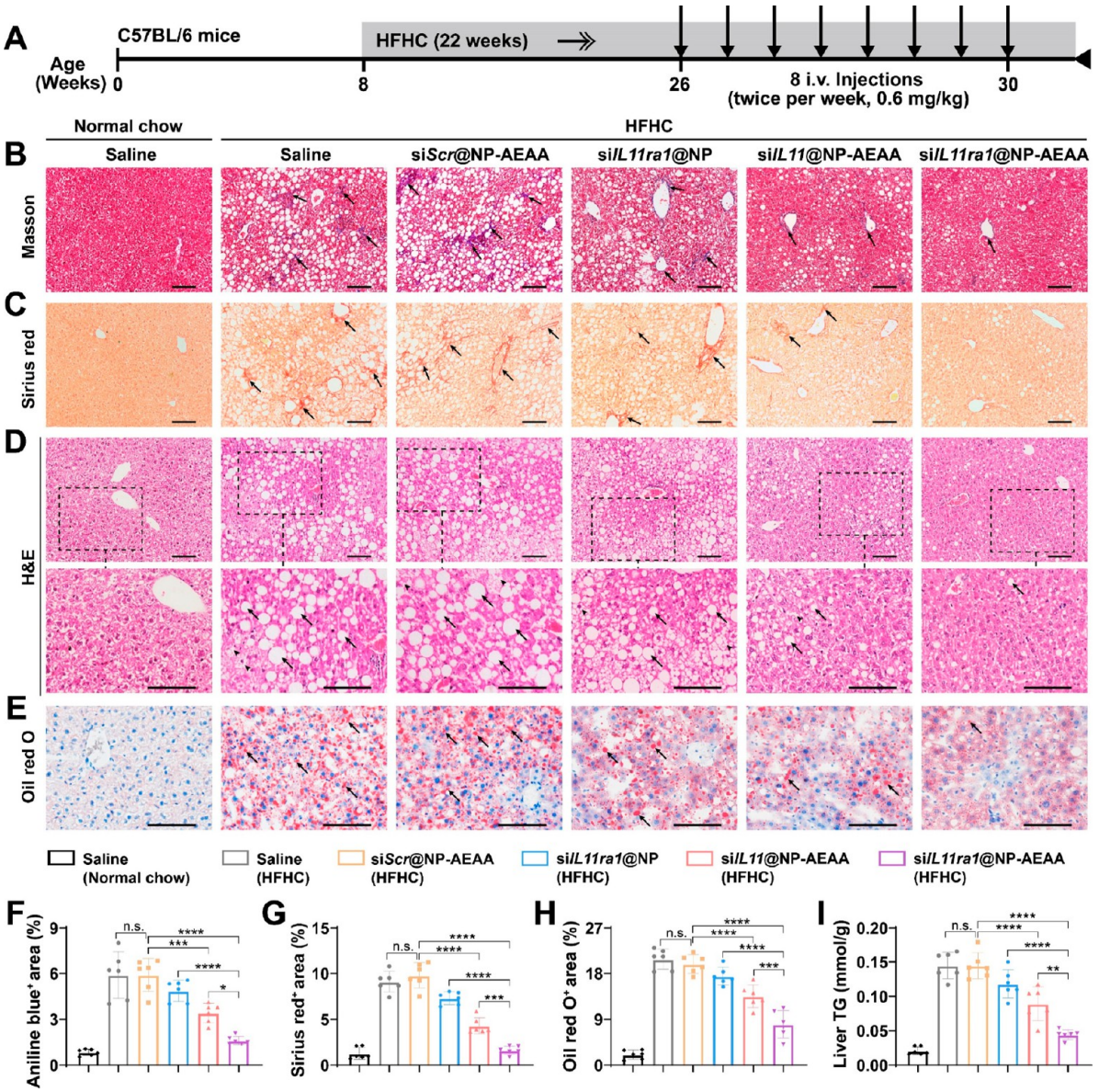

Figure 6. si*IL11ra1*@NP-AEAA shows superior therapeutic efficacy on hepatic steatosis and fibrosis in an HFHC-induced NASH model. (A) Schematic diagram of the HFHC-induced NASH model and treatment timeline for saline, si*Scr*@NP-AEAA, si*IL11ra1*@NP, si*IL11*@NP-AEAA, or si*IL11ra1*@NP-AEAA therapy. (B–E) Representative microscopic images of Masson's trichrome staining (collagen fibers are stained blue; muscle tissue is stained red) (B), Sirius red staining (collagen I and III fibers are red) (C), H&E staining (micro- and macrovesicular steatosis are indicated by the black arrowheads and black arrows, respectively) (D) and Oil red O staining (lipid droplets are stained red and indicated with black arrows) (E) of liver tissue sections obtained from normal chow-fed healthy mice, or HFHC-fed mice treated with indicated NPs. Scale bars represent 100 μm. (F–H) Quantification analysis of aniline blue-positive area (F), Sirius red-positive area (G), and Oil red O-positive area (H) in liver sections. n = 6 mice per group. (I) Quantification analysis of the hepatic triglyceride content. n = 6 mice per group. Statistical significance was determined via a one-way ANOVA with the post hoc Tukey test (F–I). Results are presented as means ± SD. *P < 0.05, **P < 0.01, ***P < 0.001, ****P < 0.0001, n.s., not significant, P > 0.05.

groups, NP-AEAA-mediated specific transfer of siRNA targeting *IL11ra1* to aHSCs showed the highest efficacy in inhibiting the expression of proinflammatory and profibrogenic genes (Figure 5E,F). In fibrotic livers, aHSCs are the primary source of tissue inhibitors of metalloproteinase 1 (TIMP1) production.[18] The balance of TIMP1 and matrix metalloproteinase 2 (MMP2) expression was disrupted in livers of HFCMCD mice with increased *Timp1*/*Mmp2* ratio (Figure 5G), indicating an abnormal ECM accumulation.[42,43] Treatment with si*IL11ra1*@NP-AEAA in vivo restored the ratio to the similar levels seen in normal chow-fed healthy mice, while both si*IL11ra1*@NP and si*IL11*@NP-AEAA had a reduced antifibrotic effect in comparison (Figure 5G). The level of hydroxyproline, a major component of fibrillar collagen, was found to be the lowest in HFCMCD mice receiving si*IL11ra1*@NP-AEAA, decreasing from 625 μg/g (si*Scr*@NP-AEAA) to 348 μg/g in wet liver tissues (Figure 5H).

Western blotting analysis of liver homogenates demonstrated that the elevated expression of IL-11 and IL11RA1 in livers of HFCMCD mice was effectively diminished following treatment with si*IL11*@NP-AEAA and si*IL11ra1*@NP-AEAA. This was accompanied by a substantial reduction in the expression of ACTA2 and COL1A1 (Figure 5I and Figure S21). Consistent with the Western blotting results observed in

https://doi.org/10.1021/acsnano.3c03217
ACS Nano 2023, 17, 14852–14870

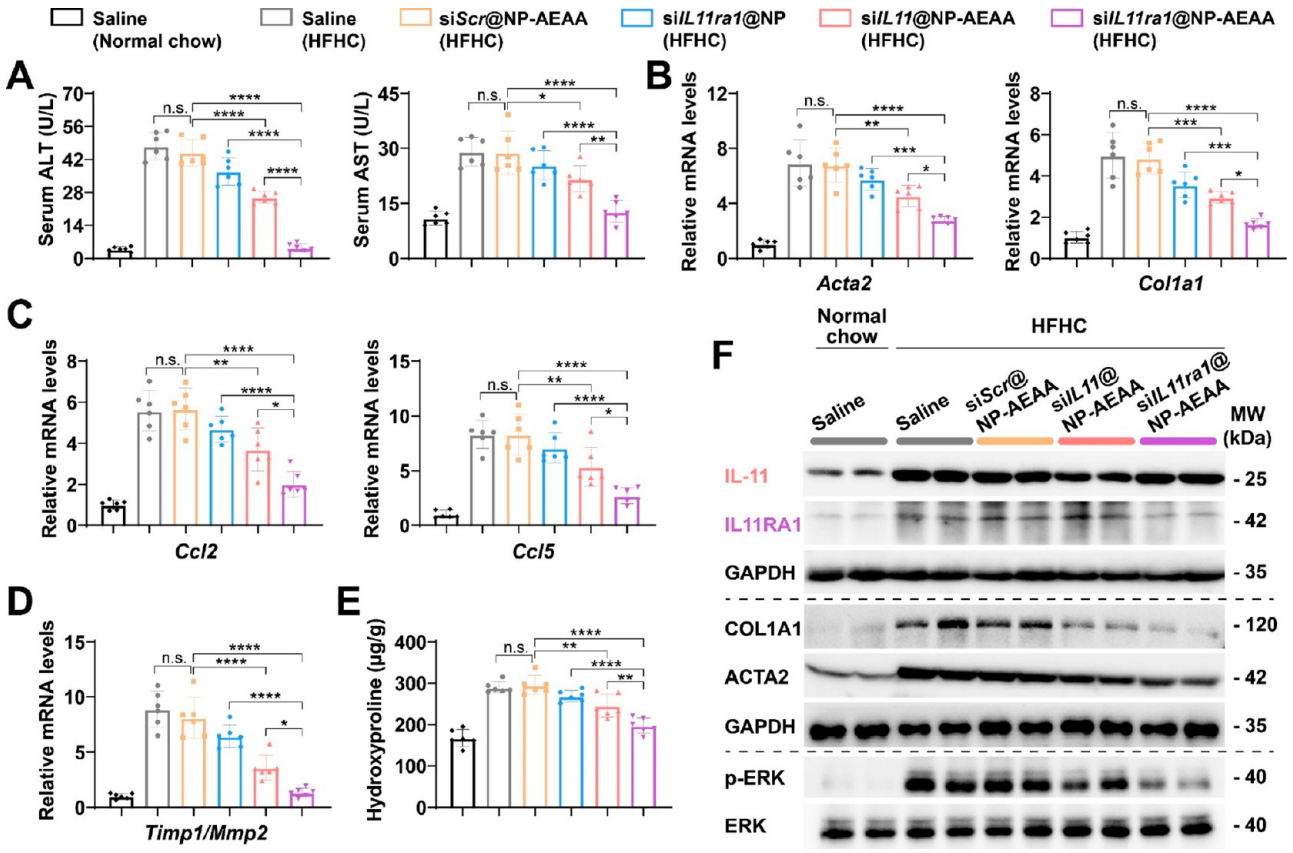

Figure 7. si*IL11ra1*@NP-AEAA shows superior therapeutic efficacy on hepatic fibrosis and inflammation in an HFHC-induced NASH model. (A) ALT and AST levels in serum. n = 6 mice per group. (B, C) Hepatic mRNA expression of profibrogenic (*Acta2*, *Col1a1*) (B) and proinflammatory (*Ccl2*, *Ccl5*) genes (C) following indicated treatments. n = 6 mice per group. (D) Relative mRNA expression of *Timp1*/*Mmp2* in livers of HFHC mice receiving the indicated treatments. n = 6 mice per group. (E) Quantification analysis of liver hydroxyproline content. n = 6 mice per group. (F) Western blots of IL-11, IL11RA1, COL1A1, ACTA2, phosphorylation, and total expression of ERK in the livers collected from the indicated groups. n = 2 mice per group. GAPDH was used as a loading control to normalize protein levels. Statistical significance was determined via a one-way ANOVA with post hoc Tukey test (A–E). Results are presented as means ± SD. *P < 0.05, **P < 0.01, ***P < 0.001, ****P < 0.0001, n.s., not significant, P > 0.05.

vitro (Figure 4D), both treatments were shown to inhibit pathological ERK activation in NASH livers, with si*IL11ra1*@NP-AEAA exhibiting the lowest expression levels of ACTA2, COL1A1, and p-ERK (Figure 5I and Figure S21). To further validate HSC-specific silence activity of NP-AEAA, we also conducted Western blotting experiments to study NP-mediated down-regulation of IL-11 or IL11RA1 in HSCs isolated from HFCMCD-fed mice with liver fibrosis. The results showed that the targeted si*IL11*@NP-AEAA significantly reduced IL-11 expression level to 38.7% in HSCs compared with saline and si*Scr*@NP-AEAA controls, but the nontargeted si*IL11*@NP treatment did not (Figure S22A,B). Similarly, treatment with si*IL11ra1*@NP-AEAA in vivo resulted in the lowest IL11RA1 expression in HSCs, which was decreased by 72.7%, 70.7%, and 74.4% compared with saline, si*Scr*@NP-AEAA, and si*IL11ra1*@NP, respectively (Figure S22C,D). These results imply that NP-AEAA-formulated siRNA targeting IL-11 signaling in aHSCs effectively suppress HSC activation, inflammation, and ECM deposition in an HFCMCD-induced NASH model. si*IL11-ra1*@NP-AEAA exhibits a superior effect over si*IL11*@NP-AEAA, probably due to its more potent inhibition of IL-11-dependent ERK activation.

si*IL11ra1*@NP-AEAA Ameliorates Steatosis, Inflammation, and Fibrosis in an HFHC-Induced NASH Model. Feeding with an HFHC diet elicits profound hepatic steatosis, ballooning, inflammation, and fibrosis (Figure S23), which mirrors the pathogenesis of human NASH and thus was used as another clinically relevant model for in vivo efficacy evaluation.[44] The NP treatment scheme for HFHC-induced model mice is depicted in Figure 6A. Histopathological analysis of liver sections showed increased fibrotic regions along with micro- and macrovesicular lipid deposition in HFHC mice receiving saline or si*Scr*@NP-AEAA treatment compared with the healthy controls (Figure 6B–H). All these hepatic lesion characteristics were attenuated in mice treated with nontargeted NP- or targeted NP-AEAA-formulated siRNA therapeutics. Relative to nontargeted si*IL11ra1*@NP, both targeted si*IL11*@NP-AEAA and si*IL11ra1*@NP-AEAA treatments substantially reduced the aniline blue- or Sirius red-stained fibrotic area, micro- and macrovesicular steatosis, as well as Oil red O-stained lipid droplets in liver tissues, with the best therapeutic efficacy achieved by si*IL11ra1*@NP-AEAA (Figure 6B–H). Similar to the Oil red O staining results, si*IL11ra1*@NP-AEAA treatment most effectively decreased the liver triglyceride content in HFHC mice among all the test groups (Figure 6I).

HFHC mice receiving saline or si*Scr*@NP-AEAA treatment were characterized with elevated serum ALT and AST levels, enhanced expression of profibrogenic (*Acta2*, *Col1a1*) and

https://doi.org/10.1021/acsnano.3c03217
ACS Nano 2023, 17, 14852–14870

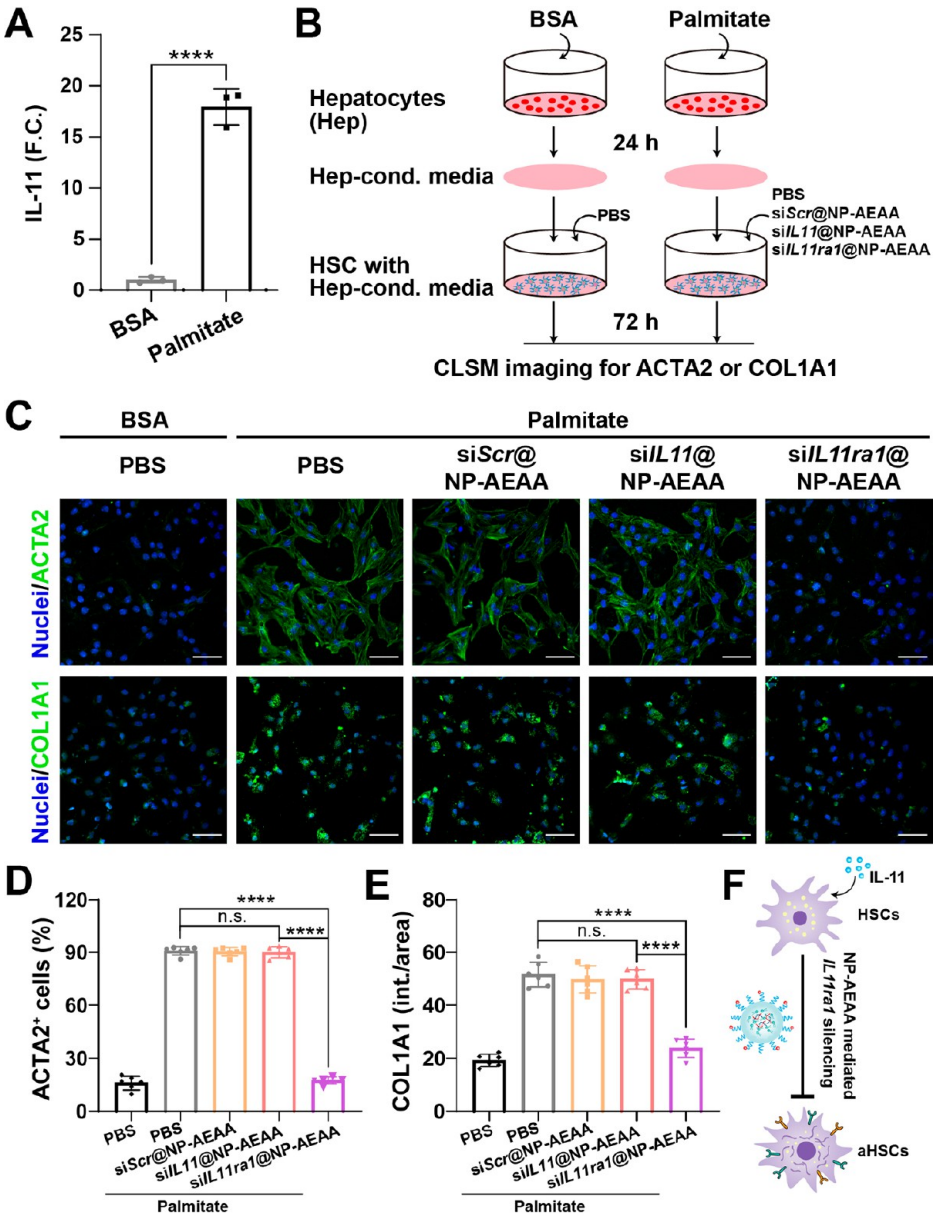

Figure 8. si*IL11ra1*@NP-AEAA inhibits paracrine IL-11-induced HSC activation. (A) ELISA assay of the IL-11 protein secreted from lipotoxic hepatocytes. Primary hepatocytes treated with free BSA served as the negative control (n = 3). (B) Schematic diagram of medium transfer experiments where HSCs were incubated with supernatant from palmitate-loaded primary hepatocytes for 48 h in the presence of PBS, si*Scr*@NP-AEAA, si*IL11*@NP-AEAA, or si*IL11ra1*@NP-AEAA. HSCs incubated with conditioned medium from BSA-treated hepatocytes were considered the "baseline" condition. (C) Representative images of ACTA2 and COL1A1 immunostaining in HSCs for experiment shown in Figure 8B. Scale bars represent 50 μm. (D, E) Quantification analysis of ACTA2$^+$ cells (D) and COL1A1 immunofluorescence intensity (E) in HSCs as shown in Figure 8C. n = 3. Images from two randomly selected fields per well were acquired, and three independent wells were measured, resulting in a total of six measurements. (F) Schematic illustration of si*IL11ra1*@NP-AEAA inhibiting HSC activation induced by paracrine IL-11 signals. Statistical significance was determined via a two-tailed unpaired Student's t test (A) and a one-way ANOVA with post hoc Tukey test (D, E). Results are presented as means ± SD. ****P < 0.0001, n.s., not significant, P > 0.05.

proinflammatory (*Ccl2*, *Ccl5*) genes, as well as increased *Timp1*/*Mmp2* ratio, and hydroxyproline content in liver homogenates, all of which were ameliorated in animals receiving NP- or NP-AEAA-formulated siRNA therapeutics (Figure 7A–E). In particular, si*IL11ra1*@NP-AEAA therapy reversed the liver damage biomarkers of ALT and AST, and fibrogenesis-associated *Timp1*/*Mmp2* ratio to normal levels (Figure 7A,D), indicative of liver function recovery and favorable ECM remodeling.

Consistent with the HFCMCD-induced NASH model, Western blotting results showed that the upregulation of IL-11 and IL11RA1 in livers of HFHC mice was effectively suppressed after si*IL11*@NP-AEAA and si*IL11ra1*@NP-AEAA treatment along with a reduction in the expression of ACTA2, COL1A1, and p-ERK (Figure 7F). Similarly, HFHC mice treated with si*IL11ra1*@NP-AEAA exhibited the lowest expression levels of ACTA2, COL1A1, and p-ERK in the liver (Figure 7F). These results reveal that NP-AEAA-aided siRNA therapeutics against IL-11 signaling in aHSCs

https://doi.org/10.1021/acsnano.3c03217
ACS Nano 2023, 17, 14852–14870

effectively inhibit HSC activation, hepatic steatosis, inflammation, and fibrosis in an HFHC-induced NASH model. The superior therapeutic effect of si*IL11ra1*@NP-AEAA is likely attributed to its potency in inhibiting IL-11-dependent ERK activation.

The biological safety of NPs was evaluated by biochemical parameters and pathological section analysis in HFHC-induced mice after the last administration. As shown in Figure S24, neither proposed siRNA therapeutics caused a pathological abnormality in the major organs (including heart, spleen, lung, and kidney) nor induced any significant changes in organ coefficient, blood urea nitrogen (BUN) or serum creatinine (CRE) compared with the healthy controls, suggesting negligible systemic toxicity within the treatment period.

Inhibition of Paracrine IL-11-Induced HSC Activation by si*IL11ra1*@NP-AEAA. Hepatocyte lipotoxicity is considered as an initiating pathophysiology of NASH, and it is associated with cytokine release.[10] We hypothesized that secretion of cytokine from lipotoxic hepatocytes could activate HSCs through paracrine signaling. This mechanism could potentially explain the discrepancy between the therapeutic efficacy of si*IL11*@NP-AEAA and si*IL11ra1*@NP-AEAA treatments in two murine models of NASH. To evaluate our hypothesis, primary hepatocytes were isolated from normal chow-fed mice and loaded with palmitate to induce lipotoxicity.[45] As shown in Figure 8A, a large amount of IL-11 was detected from supernatants of palmitate-treated hepatocytes (18-fold higher than the BSA control), indicating that hepatocytes secrete IL-11 in response to lipid overload. We then treated HSCs with conditioned medium derived from control or palmitate-loaded hepatocytes, as illustrated in Figure 8B. Immunofluorescence staining showed that medium from lipid-laden hepatocytes led to a noticeable increase in the expression of ACTA2 and COL1A1 in HSCs when treated with PBS or si*Scr*@NP-AEAA (Figure 8C–E). NP-AEAA mediated silencing of *IL-11* in HSCs did not block ACTA2 and COL1A1 expression, while si*IL11ra1*@NP-AEAA treatment reversed the percentage of $ACTA2^+$ cells and COL1A1 immunofluorescence intensity to baseline levels (Figure 8C–F). These results reveal that NP-AEAA-formulated siRNA therapeutics targeting *IL11ra1* can reverse HSC transformation and collagen deposition induced by paracrine IL-11 from lipotoxic hepatocytes, thus elucidating why si*IL11ra1*@NP-AEAA is more effective in two murine NASH models.

DISCUSSION

NASH is a form of progressive nonalcoholic fatty liver disease (NAFLD) that is characterized by hepatic lipid accumulation and inflammation. Approximately one-third of NASH patients will develop fibrosis.[46] Severe fibrosis in NASH eventually leads to cirrhosis, liver failure, and hepatocellular carcinoma, and NASH is on track to become the leading cause of liver transplantation.[47] Enormous effort has been invested to treat steatosis/hepatitis, but unfortunately there are currently no effective therapeutics approved for clinical use against NASH.[48] Additionally, only very few approaches targeting fibrogenic pathways have been explored, especially after simtuzumab (an anti-LOXL2 monoclonal antibody) and selonsertib (a selective inhibitor of ASK1) failed in phase II and III trials, respectively.[48−50]

Although the exact mechanisms underlying NASH pathogenesis are yet to be fully understood, it is widely accepted that HSC activation represents a key step in liver fibrosis since aHSCs are the major source of ECM components and profibrogenic cytokines.[51] Recent studies have indicated that overexpression of IL-11 and IL11ra1 by aHSCs are closely associated with ERK-driven myofibroblast transformation and ECM production that are involved in NASH pathology.[23] These findings, combined with our immunohistochemistry and Western blotting results, bring to the forefront IL-11 and IL11ra1 as promising targets, and our developed aHSC-targeting NP-mediated silencing of the IL-11 signaling pathway may provide insights into the treatment of NASH and related hepatic fibrosis.

RNAi-based approaches leveraging the IL-11-mediated signaling pathway represent attractive options for combating fibrotic liver diseases, but the translational potential is limited by the lack of delivery platforms that enable the specific transfer of siRNA therapeutics to aHSCs. Efforts have been made to develop targeted siRNA delivery systems for the treatment of hepatic fibrosis.[52−54] Examples include VA-coupled liposomes that target the RBP receptor,[52] pPB peptide-modified lipid nanoparticles (LNPs) that recognize the platelet-derived growth factor receptor β (PDGFR-β) receptor,[53] and polymer conjugates that target the CD44 receptor.[54] However, most of these delivery systems lack specificity and have not been fully investigated in clinically relevant NASH models. To the best of our knowledge, NP-aided delivery of siRNA to aHSCs in the fibrotic NASH liver with high selectivity has been rarely reported. In this study, we constructed a lipid-polymer hybrid NP platform using our previously reported lipid-like compound G0-C14 and copolymer PLGA-PEG conjugates for delivery of si*IL11* or si*IL11ra1*, which combines the benefits of both lipid and polymer systems to address barriers associated with siRNA delivery while overcoming some of their disadvantages. We further functionalized the NPs with aHSC-targeting moieties to specifically deliver siRNA therapeutics to aHSCs in the liver. Additionally, considering that HSCs are located within the Disse space adjacent to liver sinusoidal endothelial cells (LSECs) that limits access to larger NPs, we formulated siRNA-loaded NPs using a microfluidic approach to allow for precise tuning of NP properties, including particle size, PDI and stability. The resultant NPs have an average size of ∼85 nm, the preferred size range that facilitates NP penetration across the fenestrations of LSECs (about 50−200 nm) and subsequent entry into the aHSCs.[55]

Note that BMS-986263 (ND L02-s0201), a VA-coupled liposome containing siRNA against heat shock protein 47 (HSP47, a collagen-specific chaperone),[56] is the only HSC-targeting nanoparticle tested in clinical trials. This targeting approach exploits the fact that HSCs take up and store VA via the RBP receptor. Intriguingly, the data reported here demonstrate that compared with VA-modified NP, more NP-AEAA accumulates within fibrotic livers and is primarily colocalized with Sig-1R. Our in vivo results reveal that Sig-1R is highly expressed by aHSCs in fibrotic NASH livers but barely detectable in healthy livers, indicating that NP-AEAA can specifically target aHSCs via the AEAA-Sig-1R interaction.

We next evaluated the therapeutic potential of NP-AEAA incorporating siRNA against *IL11* (si*IL11*@NP-AEAA) or *IL11ra1* (si*IL11ra1*@NP-AEAA). Stimulation with various NASH factors (including TGF-β1, bFGF, PDGF, and H_2O_2) promotes HSC differentiation, migration, and invasion and ECM deposition, which are remarkedly inhibited by both si*IL11*@NP-AEAA and si*IL11ra1*@NP-AEAA treatment. In

https://doi.org/10.1021/acsnano.3c03217
ACS Nano 2023, 17, 14852−14870

contrast, si*IL11*@NP-AEAA shows marginal effects on HSC activation and ECM production that are induced by stimulation with IL-11 secreted from lipotoxic hepatocytes whereas si*IL11ra1*@NP-AEAA exerts potent antifibrotic effects.

We investigated the in vivo therapeutic effects of si*IL11*@NP-AEAA and si*IL11ra1*@NP-AEAA in two well-established murine models of NASH induced by HFCMCD and HFHC diets. In the HFCMCD model, methionine- and choline-deficiency inhibits the production of very low-density lipoprotein (VLDL) that is required for triglyceride export from the liver, and thereby leads to rapid liver fat accumulation when combined with a high-fat diet.[57,58] This model mimics histopathological features of NASH with steatosis, liver cell death, inflammation, and fibrosis but notably is not related to the pathogenesis of human NASH due to nutritional deficiency. The data reported here reveals that si*IL11ra1*@NP-AEAA significantly reduces fibrosis and inflammation compared with si*IL11*@NP-AEAA and nontargeted si*IL11ra1*@NP, but does not improve steatosis in the HFCMCD model, most likely due to the fact that HFCMCD-induced steatosis is driven by artificial means. To gather additional data toward a more well-rounded picture of this disease, we included another mouse HFHC model in our study. In the HFHC model, a chronic high-fat and high-cholesterol diet feeding increases de novo lipogenesis flux and causes steatosis, which is similar to that observed in NASH patients.[44,59] Consistent with the results observed in the HFCMCD model, si*IL11ra1*@NP-AEAA treatment markedly suppressed HSC differentiation and reduced the production of proinflammatory and profibrotic factors in NASH livers of HFHC mice, leading to restoration of liver structure and function. Additionally, si*IL11ra1*@NP-AEAA treatment ameliorates liver steatosis, showing disease-modifying activity. The superior therapeutic effects of si*IL11ra1*@NP-AEAA in both murine models of NASH are attributed to the inhibition of paracrine IL-11/ERK signaling in HSCs, which could not be achieved by si*IL11*@NP-AEAA. Taken together, a targeted nanoparticulate siRNA therapeutic that blocks the IL-11/ERK pathway by downregulating IL11ra1 expression in aHSCs is demonstrated to attenuate the development of NASH and related fibrosis in multiple murine models.

It is worth noting that this aHSC-targeting NP platform can be extended to the delivery of multiple RNA therapeutics (e.g., mRNA and microRNA) involved in different profibrotic pathways to provide synergistic benefits for fibrotic liver diseases. Considering that cancer-related fibrosis is characterized by excessive collagen production and ECM accumulation, this aHSC-targeting si*IL11ra1*@NP-AEAA can also be utilized as a "lead drug" for reversing the fibrotic tumor microenvironment to improve subsequent anticancer drug penetration, which may provide insights into the treatment of liver metastasis.

STUDY LIMITATIONS

Despite the encouraging results, the present study is limited to diet-induced murine models of NASH and lacks investigations in different animal species (e.g., minipigs and nonhuman primates) that resemble pathologic features of human NASH. The evaluation of therapeutic efficacy on animal models presenting with different stages of fibrosis should be included to further validate this strategy for potential translation. Additionally, optimizing the sequence of si*IL11ra1* and using AEAA- conjugated chemically modified si*IL11ra1* may be potential solutions to reduce the dosing frequency and enhance potency and specificity, especially for chronic diseases like NASH that generally require continuous long-term treatment. Given that IL-11 is a critical profibrotic effector that mediates HSC transformation and ECM deposition, it remains to be explored whether this methodology can also be applied to other liver fibroses/cirrhoses of different etiologies such as chronic viral hepatitis, cholestatic and alcoholic liver disease.

CONCLUSIONS

In conclusion, we present a robust NP platform that enables aHSC-targeting delivery of siRNA against the IL-11 signaling pathway and investigated its therapeutic effect in HFCMCD- and HFHC- induced murine models of NASH as a proof-of-concept. This work demonstrates the promising translational potential of siRNA-based therapy for NASH and other liver diseases including related hepatic fibroses and liver metastases.

EXPERIMENTAL SECTION

Mouse Model Establishment. Male C57BL/6J mice at the age of 7 weeks were purchased from the Beijing Vital River. All animal experiments were approved by the Institutional Animal Care and Use Committee of Shanghai Jiao Tong University. All mice were housed at a temperature of 25 ± 2 °C under a 12-h light/dark cycle with 40−60% humidity for 1 week before experiments and allowed free access to water and standard chow.

In the HFCMCD model, 8-week-old C57BL/6J mice received either an HFCMCD diet (methionine- and choline-deficient diet supplemented with 1% cholesterol and 46 kcal% fat; TP3622655, TrophicDiet) or normal chow (TP3622645C, TrophicDiet) ad libitum for a total of 12 weeks. In the HFHC model, 8-week-old C57BL/6J mice received either an HFHC diet (containing 40% fat and 2% cholesterol; TP2834040, TrophicDiet) or normal chow (TP2834020C1, TrophicDiet) ad libitum for a total of 22 weeks. In both NASH models, littermate mice fed with normal chow were used as healthy controls.

Synthesis and Characterization of Cationic Lipid Compound G0-C14. G0-C14 was synthesized by reacting poly(amidoamine) (PAMAM) dendrimer generation 0 with 1,2-epoxytetradecane according to a previously described procedure.[27] In brief, PAMAM dendrimer G0 and 1,2 epoxytetradecane were mixed at a molar ratio of 1:6 and stirred at 90 °C for 2 d. The reaction mixture was purified by column chromatography on silica gel (CH_2Cl_2/MeOH/NH_4OH = 75/22/3 v/v/v), yielding a final product with three fewer tails than the total possible for a designated amine monomer. ^{1}H NMR (400 MHz, Chloroform-*d*): δ 4.57 (s, 8H), 3.67−2.25 (m, 51H), 1.62−0.96 (m, 106H), 0.87 (t, J = 6.6 Hz, 15H).

Synthesis and Characterization of Targeting Polymeric Excipients. *PLGA-PEG-VA.* We first synthesized carboxyl-terminated PLGA-PEG (PLGA-PEG-COOH) by conjugating NH_2-PEG-COOH with PLGA according to our previously reported procedure.[60] Briefly, PLGA (5 μmol) and EDC·HCl (0.05 mmol) were dissolved in 1.5 mL of anhydrous DCM, and then 10 μL of NHS (0.05 mmol) dissolved in anhydrous DMSO was added to activate carboxyl groups. After the mixture was stirred at room temperature for 2 h, PLGA-NHS was obtained by precipitating in cold methanol/diethyl ether (50/50 v/v) and dried under vacuum. In the following reactions, PLGA-NHS and NH_2-PEG-COOH were dissolved in 2 mL of anhydrous DCM, and then 10 μL of DIPEA was added. The mixture was stirred at room temperature for 24 h. PLGA-PEG-COOH was obtained by precipitation in cold methanol/diethyl ether (50/50 v/v), further washed three times, and dried under vacuum. The obtained PLGA-PEG-COOH was reacted with the hydroxyl group of VA to yield VA-conjugated PLGA-PEG (PLGA-PEG-VA). In brief, PLGA-

https://doi.org/10.1021/acsnano.3c03217
ACS Nano 2023, 17, 14852−14870

PEG-COOH (5 μmol), vitamin A (10 μmol), DMAP (25 μmol), and EDC·HCl (25 μmol) were dissolved in 1.5 mL of anhydrous DCM and stirred in the dark at 60 °C for 24 h. PLGA-PEG-VA was obtained by purification in cold methanol/diethyl ether (50/50 v/v) three times and dried under a vacuum for further use. Yield: 90.2%. The ^{1}H NMR spectrum of PLGA-PEG-COOH is shown in Figure S6. ^{1}H NMR (400 MHz, Chloroform-*d*): δ 5.29−5.08 (m, 307H), 4.97−4.52 (m, 591H), 3.62 (s, 304H), 1.66−1.50 (m, 996H). VA attachment and the amount of VA attached to PLGA-PEG-COOH were determined by UV−vis at an absorbance of 328 nm.

PLGA-PEG-AEAA. 2-Bromoethylamine hydrobromide (2 mmol) was dissolved in 25 mL of acetonitrile, and the mixture was stirred for 30 min at room temperature. Then, 4-methoxybenzoyl chloride (2 mmol) was added slowly into the above solution and the mixture was reacted for 12 h. After that, t-Boc-NH-PEG-NH_2 was added, and the samples were stirred at 70 °C for 24 h. The solution was then precipitated in diethyl ether and dried under vacuum. The obtained tBoc-NH-PEG-AEAA was further dissolved in 0.5 mL of DCM/TFA solution (1/1 v/v) and stirred at room temperature for 1 h. Finally, AEAA-conjugated NH_2-PEG (NH_2-PEG-AEAA) was purified by precipitation in diethyl ether two times and dried under vacuum. Using a similar synthesis procedure to that of PLGA-PEG-COOH, we first prepared the active NHS ester of carboxyl-terminated PLGA in the presence of NHS and EDC, followed by an amide coupling reaction with the obtained NH_2-PEG-AEAA. The yielded AEAA-conjugated PLGA-PEG (PLGA-PEG-AEAA) was purified in cold methanol/diethyl ether three times and dried under vacuum for further use. Yield: 90.1%. ^{1}H NMR (400 MHz, Chloroform-*d*): δ 7.40 (d, *J* = 6.8 Hz, 2H), 7.16 (d, *J* = 9.4 Hz, 2H), 5.28−5.05 (m, 301H), 4.91−4.61 (m, 570H), 3.82−3.79 (m, 2H), 3.77−3.75 (m, 2H), 3.62 (s, 300H), 1.66−1.50 (m, 1136H).

siRNA Complexation Ability of G0-C14. To evaluate the siRNA complexation ability of G0-C14, a series of G0-C14 solutions with different concentrations were prepared. Then, 5 μL of siRNA (100 nM) was added into 20 μL of the above G0-C14 solutions, and the complexes were incubated for 20 min at room temperature. The complexes were mixed with loading dye and subjected to electrophoresis in 1% agarose gel for 15 min at 110 V. Meanwhile, naked siRNA was used as the negative control. Finally, the mobility of siRNA was visualized in a ChemiDoc Touch Imaging System (Bio-Rad, USA).

Preparation of siRNA-Loaded NPs. PLGA-PEG and Cy5.5-labeled PLGA-PEG (PLGA-PEG-Cy5.5) were synthesized by coupling NH_2-PEG-OCH_3 or NH_2-PEG-Cy5.5 to the C terminus of PLGA based on the above procedure.[60] The synthesis route of PLGA-PEG is shown in Figure S8.

siRNA-loaded NPs with different targeting polymeric excipients were prepared using a microfluidic device. For nontargeted siRNA@NP, lipid components containing PLGA-PEG/G0-C14 (1/1, w/w) were dissolved in *N*,*N*-dimethylformamide (DMF) to a total lipid concentration of 10 mM and loaded into an organic phase syringe. The siRNA was diluted in a 50 mM citrate buffer (pH = 3.0) and loaded into an aqueous phase syringe. The organic phase and aqueous phase were mixed using a microfluidic device (Micro&Nano, China) at a total flow rate of 12 mL/min. The resulting solution was kept at room temperature for 20 min to stabilize, and subsequently dialyzed against PBS (pH = 7.4) for 2 h to remove organic solvent. Based on this established procedure, we constructed targeted siRNA@NP-VA and siRNA@NP-AEAA using different weight ratios of polymeric excipients for cellular internalization and in vivo distribution. For targeted siRNA@NP-VA, 2.5%, 5%, or 10% w/w PLGA-PEG was replaced with PLGA-PEG-VA to yield siRNA@NP-$VA^{2.5\%}$, siRNA@NP-$VA^{5\%}$, and siRNA@NP-$VA^{10\%}$, respectively. For targeted siRNA@NP-AEAA, 2.5%, 5%, or 10% (w/w) PLGA-PEG was replaced with PLGA-PEG-AEAA to yield siRNA@NP-$AEAA^{2.5\%}$, siRNA@NP-$AEAA^{5\%}$, and siRNA@NP-$AEAA^{10\%}$, respectively. For Cy5.5-labeled NP, 10% w/w of PLGA-PEG was replaced with PLGA-PEG-Cy5.5 during the self-assembly process to produce Cy5.5-labeled NP with different polymeric excipients. For ^{FAM}siRNA encapsulated and Cy5.5-labeled NP, 10% w/w PLGA-PEG was replaced with PLGA-PEG-Cy5.5, and FAM-labeled siRNA was used instead of siRNA during NP preparation to produce double fluorescently labeled NP. The sequences of siRNAs used in this study were displayed as follows: *IL11*-targeting siRNA (si*IL11*): 5′-GCU GUU CUC CUA ACC CGA UdTdT-3′ (sense strand) and 5′-AUC GGG UUA GGA GAA CAG CdTdT-3′ (antisense strand); *IL11ra1*-targeting siRNA (si*IL11ra1*): 5′-GGG AAU CUU CUC UUG CCU UdTdT-3′ (sense strand) and 5′-AAG GCA AGA GAA GAU UCC CdTdT-3′ (antisense strand); scrambled siRNA (si*Scr*): 5′-UUC UCC GAA CGU GUC ACG UdTdT-3′ (sense strand) and 5′-ACG UGA CAC GUU CGG AGA AdTdT-3′ (antisense strand); FAM-labeled siRNA was synthesized by attaching the FAM dye to both the sense and antisense strands of scrambled siRNA.

Physicochemical Characterization of siRNA-Loaded NPs. The average particle diameter and zeta potential of various siRNA-loaded NPs were measured using a ZetaSizer dynamic light-scattering analyzer (Malvern, UK). Each sample was adjusted to a concentration of 0.1 mg/mL and equilibrated for 5 min at 25 °C before measurements were taken.

Encapsulation efficiency (EE) of siRNA was determined using the Quant-iT RiboGreen kit (Invitrogen, USA). Briefly, siRNA-loaded NPs were incubated with 1X TE buffer in the presence or absence of 2% Triton X-100 and vortexed for 3 min. For the high-range calibration curve, a series of RNA standard solutions were prepared at designated concentrations. NP samples and RNA standards were mixed with a 200-fold dilution of the RiboGreen reagent for 5 min at room temperature. The fluorescence intensity was measured by the Multimode Fluorescence Microplate Reader (Ex/Em: 480/520 nm, Tecan, Switzerland). NP samples treated with 2% Triton X-100 represent the total siRNA content, while untreated samples represent the free siRNA content. The EE (%) was calculated from the following equation:

$$\text{EE (\%)} = (\text{total siRNA content} - \text{free siRNA content}) / (\text{total siRNA content}) \times 100\%$$

For morphological observation, siRNA@NP and siRNA@NP-AEAA were dropped onto a copper grid (300 mesh) and air-dried following staining with 1% phosphotungstic acid for 2 min. After that, the air-dried samples were observed under TEM (Thermo Scientific, USA).

In Vitro Stability. To evaluate the serum stability of siRNA@NP-AEAA, 40 μL of siRNA@NP-AEAA (150 nM siRNA) was incubated with 10 μL of FBS in a 37 °C water bath and collected at predetermined time intervals (0, 3, 6, 12, and 24 h). Then, the obtained samples were mixed with 10 μL of EDTA (0.1 M) and heated at 85 °C for 10 min to inactivate RNase, followed by incubation with 8 μL of polyanion heparin (25 mg/mL) for 50 min at room temperature to dissociate siRNA from NPs. Subsequently, the samples underwent agarose gel electrophoresis for further analysis. Naked siRNA served as the negative control and was treated according to the same procedure.

To check the storage stability of siRNA@NP-AEAA, the freshly prepared NPs were dispersed in PBS solution (pH = 7.4) containing 20% FBS for 72 h in a 37 °C water bath. Changes in the particle size and PDI were recorded at predetermined intervals.

Cell Culture. The rat liver stellate cell line HSC-T6 (CL-0116) was purchased from Procell Life Science&Technology Co., Ltd. The NIH/3T3 cell line (GNM 6) derived from mouse embryonic fibroblasts was kindly provided by Cell Bank/Stem Cell Bank, Chinese Academy of Sciences. Primary HSCs were isolated from male C57BL/6J mice by perfusion of the liver with Pronase and collagenase,[61] followed by purification via Percoll (Yeasen, China) gradient centrifugation. qHSCs were serum-starved for 24 h and stimulated with TGF-β1 (20 ng/mL in a culture medium containing 1% FBS) for 48 h to transform into aHSCs. Primary hepatocytes were isolated from mouse livers using a modified in situ collagenase perfusion and low-speed centrifugation method.[62] Freshly isolated hepatocytes were plated onto collagen I-coated 12-well plates at a density of 5.0×10^5 cells per well. All cells were cultured in DMEM

https://doi.org/10.1021/acsnano.3c03217
ACS Nano 2023, 17, 14852−14870

medium containing 10% fetal bovine serum (FBS), 1% (v/v) penicillin, and 1% (v/v) streptomycin at 37 °C in the presence of 5% CO_2.

In Vitro Cytotoxicity and Cellular Uptake Analysis. HSC-T6, NIH/3T3, and primary mouse hepatocytes were seeded into 96-well plates at a density of 5×10^3 cells per well and maintained for 24 h. Then, the cells were treated with siRNA@NP or siRNA@NP-AEAA at different concentrations (from 10 to 500 μg/mL) in serum-free DMEM. After incubation for 24 h, 10 μL of CCK-8 was added to each well and further incubated for 1 h at 37 °C. Untreated cells were regarded as the positive control. The cell viability in each well was measured at a wavelength of 450 nm by the Multimode Fluorescence Microplate Reader (Tecan, Switzerland).

The fluorescently labeled NPs were incubated with qHSCs or aHSCs for 4 h at a siRNA concentration of 50 nM. For the competitive inhibition test, aHSCs were preincubated with excess Sig-1R antibody (30 μg/mL) for 2 h. Then, the cells were fixed in 4% paraformaldehyde, stained with DAPI (2 μg/mL), and observed by confocal microscopy (Leica, Germany). Flow cytometry (BD Biosciences, USA) was also utilized to analyze the intracellular fluorescence intensity of the collected cells.

Immunofluorescence Staining of HSCs. HSCs were seeded into 15 mm confocal dishes at a density of 3.0×10^4 cells per dish and cultured at 37 °C overnight. HSCs were then starved in serum-free DMEM for 24 h and subsequently stimulated with TGF-β1 (20 ng/mL), bFGF (30 ng/mL), PDGF (40 ng/mL), or H_2O_2 (0.2 mM) in a DMEM culture medium containing 1% FBS for an additional 48 h. HSCs without any stimulation were used as the control group. The supernatant from HSCs was assessed using an IL-11 ELISA kit to determine the amount of secreted IL-11 according to the manufacturer's protocol. For immunofluorescence staining, HSCs were fixed in 4% paraformaldehyde for 10 min, permeabilized in 0.1% Triton X-100 for 20 min, and incubated with 3% BSA for 1 h to block the nonspecific sites. After that, cells were incubated with rabbit anti-ACTA2 (1:600, Servicebio, China) or rabbit anti-COL1A1 (1:800, Servicebio, China) for 24 h at 4 °C, followed by incubation with Alexa Fluor 488-conjugated goat anti-rabbit secondary antibody (1:500, Servicebio, China) for 1 h at room temperature. After washing with PBS, cells were stained with DAPI and imaged using a confocal microscopy (Leica, Germany).

To study the efficacy of NP-AEAA formulated siRNA therapeutics on HSC activation, HSCs were treated with PBS, si*Scr*@NP-AEAA, si*IL11*@NP-AEAA, or si*IL11ra1*@NP-AEAA (50 nM siRNA) in serum-free DMEM for 4 h. Then, the culture medium was removed, and HSCs were further starved in serum-free DMEM for 20 h, followed by incubation with various NASH stimuli for an additional 48 h. HSCs treated with PBS and without any stimulation served as the "basal" state. The fluorescence images of ACTA2 and COL1A1 in HSCs were observed by confocal microscopy (Leica, Germany).

Migration and Invasion Assay. HSCs were equally seeded onto the upper side of the polycarbonate membrane coated with (for invasion assay) or without (for migration assay) Matrigel. HSCs were then treated with PBS, si*Scr*@NP-AEAA, si*IL11*@NP-AEAA, or si*IL11ra1*@NP-AEAA (50 nM siRNA) in serum-free DMEM for 4 h. Then, the culture medium was removed, and HSCs were further starved in serum-free DMEM for 20 h. Subsequently, DMEM containing TGF-β1 (20 ng/mL) and 1% FBS was added into the lower chamber to induce the migration or invasion of HSCs. After a 48-h stimulation, cotton swabs were used to gently remove cells failing in passing through the membrane. Cells that migrated or invaded toward the lower chamber were fixed in 4% paraformaldehyde and stained with crystal violet for 10 min. After that, cells were washed by PBS thrice and observed using an optical microscope (Olympus, Japan) for quantification.

In Vivo and Ex Vivo Imaging. The biodistribution of different NP formulations in HFCMCD-induced fibrotic mice was determined by an in vivo imaging system (IVIS, PerkinElmer, USA). Briefly, HFCMCD mice were randomly divided into 3 groups and intravenously injected with siRNA@$^{Cy5.5}$NP, siRNA@$^{Cy5.5}$NP-VA$^{5\%}$, or siRNA@$^{Cy5.5}$NP-AEAA$^{5\%}$ (0.6 mg/kg of siRNA), respectively. The mice were sacrificed, and heart, liver, spleen, lung, and kidneys were removed 24 h post administration. The fluorescence of each organ was assessed using an ex vivo imaging system that utilized the Cy5.5 channel across groups. To further determine the target specificity of siRNA@NP-AEAA, normal chow-fed healthy mice were injected with siRNA@$^{Cy5.5}$NP or siRNA@$^{Cy5.5}$NP-AEAA$^{5\%}$ (0.6 mg/kg of siRNA) via tail vein. After 24 h, the mice were sacrificed, and the major organs were excised for ex vivo imaging.

Immunofluorescence Analysis. To investigate cellular localization of different NPs, the collected liver tissues were fixed in neutral paraformaldehyde fixative for 24 h, dehydrated in 15% and 30% sucrose solution overnight at 4 °C, and subsequently snap frozen in the O.C.T. compound (Servicebio). Frozen liver tissues were cut into 8 μm sections and blocked with 3% BSA for 30 min at room temperature, followed by incubation with primary antibodies at 4 °C overnight. After washing with PBS three times, sections were incubated with fluorescent secondary antibodies for 50 min at room temperature, counterstained with DAPI for 5 min, then covered with a coverslip, and imaged with confocal microscopy (Leica, Germany) at the designated signal wavelength. In order to study the expression and colocalization of Sig-1R, liver sections derived from healthy control mice and untreated HFCMCD mice were performed with immunofluorescence analysis according to the procedures described above procedures. Antibodies used for immunofluorescence were listed as follows: rabbit anti-ACTA2 (1:600, Servicebio, China), mouse anti-Sig-1R (1:200, Santa Cruz, USA), CoraLite594-conjugated goat anti-rabbit secondary antibody (1:300, Proteintech, China), CoraLite594-conjugated goat anti-mouse secondary antibody (1:300, Proteintech, China), Cy5-conjugated goat anti-rabbit secondary antibody (1:800, Servicebio, China).

In Vivo Efficacy Evaluation in NASH Models. Mice receiving either HFCMCD or HFHC diet were intravenously injected with 0.15 mL of saline, si*Scr*@NP-AEAA, si*IL11ra1*@NP, si*IL11*@NP-AEAA, or si*IL11ra1*@NP-AEAA (siRNA dose of 0.6 mg/kg) twice weekly for a period of 4 weeks, following the administration schedule shown in Figure 5A and Figure 6A, respectively. All mice were sacrificed 3 days after the final injection. Blood and the main organs (heart, liver, spleen, lung, and kidney) were collected for further analysis.

Histological Analysis. For histological analysis, livers and other major tissues were fixed in neutral paraformaldehyde fixative for 48 h and embedded in paraffin and then cut into 5 μm slices, dewaxed in xylene, and hydrated with graded ethanol. Tissue slices (including heart, liver, spleen, lung, and kidney) were analyzed with hematoxylin and eosin (H&E) staining. To detect the collagen deposition in livers, liver sections were processed with Masson's trichrome staining and Sirius red staining with standard protocols. For immunohistochemistry analysis, paraffin-embedded liver sections were first treated with the corresponding primary antibodies and subsequently incubated with HRP-conjugated secondary antibodies. After washing three times, the sections were developed with 3,3′-diaminobenzidine (DAB) (brown) and counterstained with hematoxylin for clear visualization of nuclei (blue). Liver tissues embedded in O.C.T. were cut into 8 μm sections and used for Oil red O staining. The percentage of the stained fibrotic area (the blue area indicated in Masson's trichrome staining and the red area indicated in Sirius red staining), IL-11- and ACTA2-positive area, and Oil red O-positive area in each sample were calculated using the NIH ImageJ software (Bethesda, USA). Images were taken with an optical microscope (Olympus, Japan).

Colorimetric Assays. Serum alanine aminotransferase (ALT), aspartate aminotransferase (AST), blood urea nitrogen (BUN), and creatinine (CRE) levels were measured using commercially available kits according to the manufacturer's standards (Nanjing Jiancheng Bioengineering Institute, China). Total lipids were extracted from liver samples using the Folch method as previously reported,[63] and the levels of liver triglyceride were quantified using Triglyceride Assay Kit (Nanjing Jiancheng Bioengineering Institute, China). Hydroxyproline content in liver tissues was measured using a Hydroxyproline Assay kit following the manufacturer's instructions (Nanjing Jiancheng Bioengineering Institute, China).

https://doi.org/10.1021/acsnano.3c03217
ACS Nano 2023, 17, 14852−14870

Quantitative Reverse Transcription PCR (qRT-PCR) Analysis. Total RNA was isolated from the liver tissues using the RNA extraction reagent (Vazyme) and reverse transcribed into cDNA with a HiScript Q RT SuperMix Kit (Vazyme). Expression of *Acta2*, *Col1a1*, *Ccl2*, *Ccl5*, *Timp1*, and *Mmp2* was measured using ChamQ Universal SYBR qPCR Master Mix (Vazyme) on StepOnePlus Real-Time PCR System (Applied Biosystems, USA). All of the primer sequences are listed in Supplementary Table 2. The relative expression of target mRNA was analyzed by the $2^{-\Delta\Delta CT}$ method, and GAPDH was used as the internal reference.

Western Blotting. Total protein samples were extracted from HSCs or mouse livers with a RIPA lysis buffer (Beyotime) containing phosphatase and protease inhibitors (Epizyme). The protein concentration was determined using the BCA Protein Assay Kit (Share-bio). Protein samples were separated by 10% SDS-polyacrylamide gel electrophoresis and transferred to poly(vinylidene difluoride) membranes (Millipore). The membranes were blocked with a TBST buffer containing 5% skim milk for 30 min at room temperature and then incubated with primary antibodies overnight at 4 °C. Membranes were washed and incubated with conjugated secondary antibodies for 1 hour and visualized using Omni-ECL enhanced chemiluminescence (Epizyme). GAPDH was used as a loading control to normalize the levels of protein. Antibodies were rabbit anti-IL-11 (1:1000, Proteintech, China) and anti-IL11RA (1:1000, Proteintech, China), mouse anti-GAPDH (1:5000, ABclonal, China), rabbit anti-ACTA2 (1:1000, Servicebio, China) and anti-COL1A1 (1:1000, Servicebio, China), mouse anti-ERK 1/2 (1:1000, Santa Cruz, USA) and anti-p-ERK 1/2 (1:1000, Santa Cruz, USA), HRP-conjugated goat anti-mouse IgG (1:5000, Proteintech, China), and HRP-conjugated goat anti-rabbit IgG (1:5000, Signalway Antibody, USA).

Palmitate Treatment in Vitro. Primary mouse hepatocytes were starved in serum-free DMEM for 12 h and then treated with BSA-conjugated palmitate (0.5 mM) for 48 h to induce lipotoxicity. Hepatocytes treated with fatty-acid-free BSA were used as the negative control. Secreted IL-11 from hepatocytes was quantified using an ELISA kit according to the manufacture's protocol.

Inhibition Assay of Paracrine-Induced HSC Activation. To determine whether NP-AEAA formulated siRNA therapeutics could inhibit HSC activation induced by paracrine IL-11, HSCs were treated with PBS, si*Scr*@NP-AEAA, si*IL11*@NP-AEAA, or si*IL11-ra1*@NP-AEAA (50 nM siRNA) for 4 h, and starved in serum-free DMEM for 20 h. Then, HSCs were incubated with conditioned medium from BSA or palmitate-treated hepatocytes for 48 h. The fluorescence images of ACTA2 and COL1A1 expressed by HSCs were observed by confocal microscopy (Leica, Germany) and analyzed using the NIH ImageJ software (Bethesda, USA).

Statistical Analysis. All statistical data are analyzed using GraphPad Prism 8.2.1 software. Results are presented as the mean ± standard deviation (SD). The two-tailed unpaired Student's *t* test was used to determine statistical significance when only two groups were compared. For comparisons between multiple groups, one-way analysis of variance (ANOVA) with a post hoc Tukey test (when several groups were compared to each other) or Dunnett's test (when several groups were compared to one group) was used. Statistical significance was displayed as follows: $^{*}P < 0.05$, $^{**}P < 0.01$, $^{***}P < 0.001$, and $^{****}P < 0.0001$.

ASSOCIATED CONTENT

Supporting Information

The Supporting Information is available free of charge at https://pubs.acs.org/doi/10.1021/acsnano.3c03217.

Immunohistochemistry staining; synthesis route and characterization of materials; cellular uptake analysis; histopathological analysis; in vivo biodistribution evaluation; immunofluorescent staining and subcellular localization analysis; ELISA assay; immunofluorescence staining; quantitative analysis of Western blots; assessment of antifibrotic effect; Western blotting analysis; histopathological analysis; in vivo safety evaluation; characterization of NP formulations; primer sequences (PDF)

AUTHOR INFORMATION

Corresponding Authors

Xiaoyang Xu − *Department of Chemical and Materials Engineering and Department of Biomedical Engineering, New Jersey Institute of Technology, Newark, New Jersey 07102, United States;* orcid.org/0000-0002-1634-3329; Email: xiaoyang.xu@njit.edu

Xue-Qing Zhang − *Shanghai Frontiers Science Center of Drug Target Identification and Delivery, School of Pharmacy, National Key Laboratory of Innovative Immunotherapy, Shanghai Jiao Tong University, Shanghai 200240, P. R. China;* orcid.org/0000-0002-4954-2586; Email: xueqingzhang@sjtu.edu.cn

Authors

Chenshuang Zhang − *Shanghai Frontiers Science Center of Drug Target Identification and Delivery, School of Pharmacy, National Key Laboratory of Innovative Immunotherapy, Shanghai Jiao Tong University, Shanghai 200240, P. R. China*

Yilong Teng − *Shanghai Frontiers Science Center of Drug Target Identification and Delivery, School of Pharmacy, National Key Laboratory of Innovative Immunotherapy, Shanghai Jiao Tong University, Shanghai 200240, P. R. China*

Fengqiao Li − *Department of Chemical and Materials Engineering, New Jersey Institute of Technology, Newark, New Jersey 07102, United States*

William Ho − *Department of Chemical and Materials Engineering, New Jersey Institute of Technology, Newark, New Jersey 07102, United States*

Xin Bai − *Shanghai Frontiers Science Center of Drug Target Identification and Delivery, School of Pharmacy, National Key Laboratory of Innovative Immunotherapy, Shanghai Jiao Tong University, Shanghai 200240, P. R. China*

Complete contact information is available at: https://pubs.acs.org/10.1021/acsnano.3c03217

Author Contributions

X.-Q.Z., X.X., and C.Z. conceived and designed the experiments. C.Z. performed most experiments. Y.T. assisted with chemical synthesis. C.Z., F.L., Y.T., X.B., X.X., and X.-Q.Z. analyzed and discussed results. C.Z. and X.-Q.Z. wrote the paper. X.-Q.Z., X.X., C.Z., and W.H. reviewed and edited the paper.

Notes

The authors declare no competing financial interest.

ACKNOWLEDGMENTS

This work was supported by the "Open Competition to Select the Best Candidates" Key Technology Program for Nucleic Acid Drugs of NCTIB (Grant No. NCTIB2022HS02002), the Natural Science Foundation of Shanghai (23ZR1427600), Shanghai Jiao Tong University Scientific and Technological Innovation Funds (19X160020005, Grant No. 2019TPA10), Foundation of National Facility for Translational Medicine (Shanghai) (TMSK-2020-008), the Interdisciplinary Program

of Shanghai Jiao Tong University [project number ZH2018ZDA36 (19X190020006)], the National Science Foundation (2001606), and the Gustavus and Louise Pfeiffer Research Foundation Award.

REFERENCES

(1) Younossi, Z. M.; Koenig, A. B.; Abdelatif, D.; Fazel, Y.; Henry, L.; Wymer, M. Global epidemiology of nonalcoholic fatty liver disease-Meta-analytic assessment of prevalence, incidence, and outcomes. *Hepatology* **2016**, *64* (1), 73−84.
(2) Younossi, Z.; Anstee, Q. M.; Marietti, M.; Hardy, T.; Henry, L.; Eslam, M.; George, J.; Bugianesi, E. Global burden of NAFLD and NASH: trends, predictions, risk factors and prevention. *Nat. Rev. Gastroenterol. Hepatol.* **2018**, *15* (1), 11−20.
(3) Team, R.; LaBrecque, D. R.; Abbas, Z.; Anania, F.; Ferenci, P.; Khan, A. G.; Goh, K.-L.; Hamid, S. S.; Isakov, V.; Lizarzabal, M.; et al. World Gastroenterology Organisation global guidelines: Nonalcoholic fatty liver disease and nonalcoholic steatohepatitis. *J. Clin. Gastroenterol.* **2014**, *48* (6), 467−473.
(4) Bedossa, P. Pathology of non-alcoholic fatty liver disease. *Liver Int.* **2017**, *37* (Suppl. 1), 85−89.
(5) Parthasarathy, G.; Revelo, X.; Malhi, H. Pathogenesis of nonalcoholic steatohepatitis: An overview. *Hepatol. Commun.* **2020**, *4* (4), 478−492.
(6) Pellicoro, A.; Ramachandran, P.; Iredale, J. P.; Fallowfield, J. A. Liver fibrosis and repair: Immune regulation of wound healing in a solid organ. *Nat. Rev. Immunol.* **2014**, *14* (3), 181−194.
(7) Younossi, Z. M.; Stepanova, M.; Rafiq, N.; Makhlouf, H.; Younoszai, Z.; Agrawal, R.; Goodman, Z. Pathologic criteria for nonalcoholic steatohepatitis: interprotocol agreement and ability to predict liver-related mortality. *Hepatology* **2011**, *53* (6), 1874−1882.
(8) Ekstedt, M.; Hagström, H.; Nasr, P.; Fredrikson, M.; Stål, P.; Kechagias, S.; Hultcrantz, R. Fibrosis stage is the strongest predictor for disease-specific mortality in NAFLD after up to 33 years of follow-up. *Hepatology* **2015**, *61* (5), 1547−1554.
(9) Konerman, M. A.; Jones, J. C.; Harrison, S. A. Pharmacotherapy for NASH: Current and emerging. *J. Hepatol.* **2018**, *68* (2), 362−375.
(10) Friedman, S. L.; Neuschwander-Tetri, B. A.; Rinella, M.; Sanyal, A. J. Mechanisms of NAFLD development and therapeutic strategies. *Nat. Med.* **2018**, *24* (7), 908−922.
(11) Hardy, T.; Oakley, F.; Anstee, Q. M.; Day, C. P. Nonalcoholic fatty liver disease: Pathogenesis and disease spectrum. *Annu. Rev. Pathol.* **2016**, *11*, 451−496.
(12) Machado, M. V.; Diehl, A. M. Pathogenesis of nonalcoholic steatohepatitis. *Gastroenterology* **2016**, *150* (8), 1769−1777.
(13) Iwaisako, K.; Jiang, C.; Zhang, M.; Cong, M.; Moore-Morris, T. J.; Park, T. J.; Liu, X.; Xu, J.; Wang, P.; Paik, Y.-H.; et al. Origin of myofibroblasts in the fibrotic liver in mice. *Proc. Natl. Acad. Sci. U. S. A.* **2014**, *111* (32), E3297−E3305.
(14) Kisseleva, T.; Brenner, D. A. Mechanisms of fibrogenesis. *Exp. Biol. Med.* **2008**, *233* (2), 109−122.
(15) Bataller, R.; Brenner, D. A. Liver fibrosis. *J. Clin. Invest.* **2005**, *115* (2), 209−218.
(16) Oseini, A. M.; Sanyal, A. J. Therapies in non-alcoholic steatohepatitis (NASH). *Liver Int.* **2017**, *37* (Suppl 1), 97−103.
(17) Lemoinne, S.; Friedman, S. L. New and emerging anti-fibrotic therapeutics entering or already in clinical trials in chronic liver diseases. *Curr. Opin. Pharmacol.* **2019**, *49*, 60−70.
(18) Kisseleva, T.; Brenner, D. Molecular and cellular mechanisms of liver fibrosis and its regression. *Nat. Rev. Gastroenterol. Hepatol.* **2021**, *18* (3), 151−166.
(19) Tsuchida, T.; Friedman, S. L. Mechanisms of hepatic stellate cell activation. *Nat. Rev. Gastroenterol. Hepatol.* **2017**, *14*, 397−411.
(20) Cook, S. A.; Schafer, S. Hiding in plain sight: Interleukin-11 emerges as a master regulator of fibrosis, tissue integrity, and stromal inflammation. *Annu. Rev. Med.* **2020**, *71*, 263−276.
(21) Corden, B.; Adami, E.; Sweeney, M.; Schafer, S.; Cook, S. A. IL-11 in cardiac and renal fibrosis: Late to the party but a central player. *Br. J. Pharmacol.* **2020**, *177* (8), 1695−1708.
(22) Schafer, S.; Viswanathan, S.; Widjaja, A. A.; Lim, W.-W.; Moreno-Moral, A.; DeLaughter, D. M.; Ng, B.; Patone, G.; Chow, K.; Khin, E.; et al. IL-11 is a crucial determinant of cardiovascular fibrosis. *Nature* **2017**, *552*, 110−115.
(23) Widjaja, A. A.; Singh, B. K.; Adami, E.; Viswanathan, S.; Dong, J.; D'Agostino, G. A.; Ng, B.; Lim, W. W.; Tan, J.; Paleja, B. S.; et al. Inhibiting interleukin 11 signaling reduces hepatocyte death and liver fibrosis, inflammation, and steatosis in mouse models of nonalcoholic steatohepatitis. *Gastroenterology* **2019**, *157* (3), 777−792.e714.
(24) Bai, X.; Zhao, G.; Chen, Q.; Li, Z.; Gao, M.; Ho, W.; Xu, X.; Zhang, X.-Q. Inhaled siRNA nanoparticles targeting IL11 inhibit lung fibrosis and improve pulmonary function post-bleomycin challenge. *Sci. Adv.* **2022**, *8* (25), No. eabn7162.
(25) Yin, H.; Kanasty, R. L.; Eltoukhy, A. A.; Vegas, A. J.; Dorkin, J. R.; Anderson, D. G. Non-viral vectors for gene-based therapy. *Nat. Rev. Genet.* **2014**, *15* (8), 541−555.
(26) Debacker, A. J.; Voutila, J.; Catley, M.; Blakey, D.; Habib, N. Delivery of oligonucleotides to the liver with GalNAc: From research to registered therapeutic drug. *Mol. Ther.* **2020**, *28* (8), 1759−1771.
(27) Xu, X.; Xie, K.; Zhang, X.-Q.; Pridgen, E. M.; Park, G. Y.; Cui, D. S.; Shi, J.; Wu, J.; Kantoff, P. W.; Lippard, S. J.; et al. Enhancing tumor cell response to chemotherapy through nanoparticle-mediated codelivery of siRNA and cisplatin prodrug. *Proc. Natl. Acad. Sci. U.S.A.* **2013**, *110* (46), 18638−18643.
(28) Jin, Y.; Wang, H.; Yi, K.; Lv, S.; Hu, H.; Li, M.; Tao, Y. Applications of nanobiomaterials in the therapy and imaging of acute liver failure. *Nano-Micro Lett.* **2021**, *13* (1), 25.
(29) Zhang, Y.-N.; Poon, W.; Tavares, A. J.; McGilvray, I. D.; Chan, W. C. W. Nanoparticle-liver interactions: Cellular uptake and hepatobiliary elimination. *J. Controlled Release* **2016**, *240* (28), 332−348.
(30) Senoo, H.; Imai, K.; Matano, Y.; Sato, M. Molecular mechanisms in the reversible regulation of morphology, proliferation and collagen metabolism in hepatic stellate cells by the three-dimensional structure of the extracellular matrix. *J. Gastroenterol. Hepatol.* **1998**, *13* (S1), S19−S32.
(31) Hu, M.; Wang, Y.; Xu, L.; An, S.; Tang, Y.; Zhou, X.; Li, J.; Liu, R.; Huang, L. Relaxin gene delivery mitigates liver metastasis and synergizes with check point therapy. *Nat. Commun.* **2019**, *10* (1), 2993.
(32) Li, J.; He, Y.; Sun, W.; Luo, Y.; Cai, H.; Pan, Y.; Shen, M.; Xia, J.; Shi, X. Hyaluronic acid-modified hydrothermally synthesized iron oxide nanoparticles for targeted tumor MR imaging. *Biomaterials* **2014**, *35* (11), 3666−3677.
(33) Zhang, A.; Meng, K.; Liu, Y.; Pan, Y.; Qu, W.; Chen, D.; Xie, S. Absorption, distribution, metabolism, and excretion of nanocarriers in vivo and their influences. *Adv. Colloid Interface Sci.* **2020**, *284*, 102261.
(34) Poon, W.; Kingston, B. R.; Ouyang, B.; Ngo, W.; Chan, W. C. W. A framework for designing delivery systems. *Nat. Nanotechnol.* **2020**, *15*, 819−829.
(35) Han, X.; Gong, N.; Xue, L.; Billingsley, M. M.; El-Mayta, R.; Shepherd, S. J.; Alameh, M.-G.; Weissman, D.; Mitchell, M. J. Ligand-tethered lipid nanoparticles for targeted RNA delivery to treat liver fibrosis. *Nat. Commun.* **2023**, *14* (1), 75.
(36) Maher, J. J.; Bissell, D. M. Cell-matrix interactions in liver. *Semin. Cell Biol.* **1993**, *4* (3), 189−201.
(37) Olaso, E.; Friedman, S. L. Molecular regulation of hepatic fibrogenesis. *J. Hepatol.* **1998**, *29* (5), 836−847.
(38) Bissell, D Transforming growth factor beta and the liver. *Hepatology* **2001**, *34* (5), 859−867.
(39) Yang, C.; Zeisberg, M.; Mosterman, B.; Sudhakar, A.; Yerramalla, U.; Holthaus, K.; Xu, L.; Eng, F.; Afdhal, N.; Kalluri, R. Liver fibrosis: insights into migration of hepatic stellate cells in response to extracellular matrix and growth factors. *Gastroenterology* **2003**, *124* (1), 147−159.

https://doi.org/10.1021/acsnano.3c03217
ACS Nano 2023, 17, 14852−14870

(40) Kim, B.-M.; Abdelfattah, A. M.; Vasan, R.; Fuchs, B. C.; Choi, M. Y. Hepatic stellate cells secrete Ccl5 to induce hepatocyte steatosis. *Sci. Rep.* **2018**, *8* (1), 7499.
(41) Marra, F.; Tacke, F. Roles for chemokines in liver disease. *Gastroenterology* **2014**, *147* (3), 577−594.
(42) Hemmann, S.; Graf, J.; Roderfeld, M.; Roeb, E. Expression of MMPs and TIMPs in liver fibrosis - a systematic review with special emphasis on anti-fibrotic strategies. *J. Hepatol.* **2007**, *46* (5), 955−975.
(43) Iredale, J. P.; Benyon, R. C.; Pickering, J.; McCullen, M.; Northrop, M.; Pawley, S.; Hovell, C.; Arthur, M. J. Mechanisms of spontaneous resolution of rat liver fibrosis. Hepatic stellate cell apoptosis and reduced hepatic expression of metalloproteinase inhibitors. *J. Clin. Invest.* **1998**, *102* (3), 538−549.
(44) Machado, M. V.; Michelotti, G. A.; Xie, G.; Pereira, T. A.; Boursier, J.; Bohnic, B.; Guy, C. D.; Diehl, A. M. Mouse models of diet-induced nonalcoholic steatohepatitis reproduce the heterogeneity of the human disease. *PLoS One* **2015**, *10* (5), No. e0127991.
(45) Dong, J.; Viswanathan, S.; Adami, E.; Singh, B. K.; Chothani, S. P.; Ng, B.; Lim, W. W.; Zhou, J.; Tripathi, M.; Ko, N. S. J.; et al. Hepatocyte-specific IL11 cis-signaling drives lipotoxicity and underlies the transition from NAFLD to NASH. *Nat. Commun.* **2021**, *12* (1), 66.
(46) Argo, C. K.; Northup, P. G.; Al-Osaimi, A. M. S.; Caldwell, S. H. Systematic review of risk factors for fibrosis progression in non-alcoholic steatohepatitis. *J. Hepatol.* **2009**, *51* (2), 371−379.
(47) Mittal, S.; El-Serag, H. B.; Sada, Y. H.; Kanwal, F.; Duan, Z.; Temple, S.; May, S. B.; Kramer, J. R.; Richardson, P. A.; Davila, J. A. Hepatocellular carcinoma in the absence of cirrhosis in United States Veterans is associated with nonalcoholic fatty liver disease. *Clin. Gastroenterol. Hepatol.* **2016**, *14* (1), 124−131.e121.
(48) Romero, F. A.; Jones, C. T.; Xu, Y.; Fenaux, M.; Halcomb, R. L. The race to bash NASH: Emerging targets and drug development in a complex liver disease. *J. Med. Chem.* **2020**, *63* (10), 5031−5073.
(49) Harrison, S. A.; Abdelmalek, M. F.; Caldwell, S.; Shiffman, M. L.; Diehl, A. M.; Ghalib, R.; Lawitz, E. J.; Rockey, D. C.; Schall, R. A.; Jia, C.; et al. Simtuzumab is ineffective for patients with bridging fibrosis or compensated cirrhosis caused by nonalcoholic steatohepatitis. *Gastroenterology* **2018**, *155* (4), 1140−1153.
(50) Harrison, S. A.; Wong, V. W.-S.; Okanoue, T.; Bzowej, N.; Vuppalanchi, R.; Younes, Z.; Kohli, A.; Sarin, S.; Caldwell, S. H.; Alkhouri, N.; et al. Selonsertib for patients with bridging fibrosis or compensated cirrhosis due to NASH: Results from randomized phase III STELLAR trials. *J. Hepatol.* **2020**, *73* (1), 26−39.
(51) Friedman, S. L. Hepatic stellate cells: protean, multifunctional, and enigmatic cells of the liver. *Physiol. Rev.* **2008**, *88* (1), 125−172.
(52) Sato, Y.; Murase, K.; Kato, J.; Kobune, M.; Sato, T.; Kawano, Y.; Takimoto, R.; Takada, K.; Miyanishi, K.; Matsunaga, T.; et al. Resolution of liver cirrhosis using vitamin A-coupled liposomes to deliver siRNA against a collagen-specific chaperone. *Nat. Biotechnol.* **2008**, *26* (4), 431−442.
(53) Zhang, J.; Shen, H.; Xu, J.; Liu, L.; Tan, J.; Li, M.; Xu, N.; Luo, S.; Wang, J.; Yang, F.; et al. Liver-targeted siRNA lipid nanoparticles treat hepatic cirrhosis by dual antifibrotic and anti-inflammatory activities. *ACS Nano* **2020**, *14* (5), 6305−6322.
(54) Wang, Y.; Xiong, L.; Dong, Z.; Ran, K.; Bai, W.; Mo, Z.; Huang, K.; Ye, Y.; Tao, Y.; Yin, S.; et al. Autophagy-interfering nanoboat drifting along CD44-golgi-ER flow as RNAi therapeutics for hepatic fibrosis. *ACS Appl. Mater. Interfaces* **2023**, *15*, 28941.
(55) Calvente, C. J.; Sehgal, A.; Popov, Y.; Kim, Y. O.; Zevallos, V.; Sahin, U.; Diken, M.; Schuppan, D. Specific hepatic delivery of procollagen α1(I) small interfering RNA in lipid-like nanoparticles resolves liver fibrosis. *Hepatology* **2015**, *62* (4), 1285−1297.
(56) Lawitz, E. J.; Shevell, D. E.; Tirucherai, G. S.; Du, S.; Chen, W.; Kavita, U.; Coste, A.; Poordad, F.; Karsdal, M.; Nielsen, M.; et al. BMS-986263 in patients with advanced hepatic fibrosis: 36-week results from a randomized, placebo-controlled phase 2 trial. *Hepatology* **2022**, *75* (4), 912−923.
(57) Macfarlane, D. P.; Zou, X.; Andrew, R.; Morton, N. M.; Livingstone, D. E. W.; Aucott, R. L.; Nyirenda, M. J.; Iredale, J. P.; Walker, B. R. Metabolic pathways promoting intrahepatic fatty acid accumulation in methionine and choline deficiency: implications for the pathogenesis of steatohepatitis. *Am. J. Physiol.* **2011**, *300* (2), E402−E409.
(58) Ross, T. T.; Crowley, C.; Kelly, K. L.; Rinaldi, A.; Beebe, D. A.; Lech, M. P.; Martinez, R. V.; Carvajal-Gonzalez, S.; Boucher, M.; Hirenallur-Shanthappa, D.; et al. Acetyl-CoA carboxylase inhibition improves multiple dimensions of NASH pathogenesis in model systems. *Cell. Mol. Gastroenterol. Hepatol.* **2020**, *10* (4), 829−851.
(59) Lambert, J. E.; Ramos-Roman, M. A.; Browning, J. D.; Parks, E. J. Increased de novo lipogenesis is a distinct characteristic of individuals with nonalcoholic fatty liver disease. *Gastroenterology* **2014**, *146* (3), 726−735.
(60) Chen, Q.; Gao, M.; Li, Z.; Xiao, Y.; Bai, X.; Boakye-Yiadom, K. O.; Xu, X.; Zhang, X.-Q. Biodegradable nanoparticles decorated with different carbohydrates for efficient macrophage-targeted gene therapy. *J. Controlled Release* **2020**, *323*, 179−190.
(61) Mederacke, I.; Dapito, D. H.; Affò, S.; Uchinami, H.; Schwabe, R. F. High-yield and high-purity isolation of hepatic stellate cells from normal and fibrotic mouse livers. *Nat. Protoc.* **2015**, *10* (2), 305−315.
(62) Zhang, Q.; Qu, Y.; Li, Z.; Zhang, Q.; Xu, M.; Cai, X.; Li, F.; Lu, L. Isolation and culture of single cell types from rat liver. *Cells Tissues Organs* **2016**, *201* (4), 253−267.
(63) Folch, J.; Lees, M.; Stanley, G. H. S. A simple method for the isolation and purification of total lipides from animal tissues. *J. Biol. Chem.* **1957**, *226* (1), 497−509.

https://doi.org/10.1021/acsnano.3c03217
ACS Nano 2023, 17, 14852−14870